BRAIN
ORIGINAL ARTICLE

Expression of 4E-BP1 in juvenile mice alleviates mTOR-induced neuronal dysfunction and epilepsy

Lena H. Nguyen,[1,2] Youfen Xu,[1] Travorn Mahadeo,[1] Longbo Zhang,[1] Tiffany V. Lin,[1] Heather A. Born,[3,4] Anne E. Anderson[3,4] and Angélique Bordey[1,2]

Hyperactivation of the mTOR pathway during foetal neurodevelopment alters neuron structure and function, leading to focal malformation of cortical development and intractable epilepsy. Recent evidence suggests a role for dysregulated cap-dependent translation downstream of mTOR signalling in the formation of focal malformation of cortical development and seizures. However, it is unknown whether modifying translation once the developmental pathologies are established can reverse neuronal abnormalities and seizures. Addressing these issues is crucial with regards to therapeutics because these neurodevelopmental disorders are predominantly diagnosed during childhood, when patients present with symptoms. Here, we report increased phosphorylation of the mTOR effector and translational repressor, 4E-BP1, in patient focal malformation of cortical development tissue and in a mouse model of focal malformation of cortical development. Using temporally regulated conditional gene expression systems, we found that expression of a constitutively active form of 4E-BP1 that resists phosphorylation by focal malformation of cortical development in juvenile mice reduced neuronal cytomegaly and corrected several neuronal electrophysiological alterations, including depolarized resting membrane potential, irregular firing pattern and aberrant expression of HCN4 ion channels. Further, 4E-BP1 expression in juvenile focal malformation of cortical development mice after epilepsy onset resulted in improved cortical spectral activity and decreased spontaneous seizure frequency in adults. Overall, our study uncovered a remarkable plasticity of the juvenile brain that facilitates novel therapeutic opportunities to treat focal malformation of cortical development-related epilepsy during childhood with potentially long-lasting effects in adults.

1 Department of Neurosurgery, Yale University School of Medicine, New Haven, CT 06510, USA
2 Department of Cellular and Molecular Physiology, Yale University School of Medicine, New Haven, CT 06510, USA
3 Cain Foundation Laboratories, Jan and Dan Duncan Neurological Research Institute at Texas Children's Hospital, Houston, TX 77030, USA
4 Department of Pediatrics, Baylor College of Medicine, Houston, TX 77030, USA

Correspondence to: Angélique Bordey, PhD
Department of Neurosurgery, Yale University School of Medicine
310 Cedar Street, LH403 New Haven, CT 06511, USA
E-mail: angelique.bordey@yale.edu

Keywords: malformation of cortical development; seizures; cap-dependent translation; hyperpolarization-activated cyclic nucleotide-gated (HCN) channels; *in utero* electroporation

Received July 07, 2021. Revised September 01, 2021. Accepted September 22, 2021. Advance access publication November 25, 2021

Abbreviations: 4E-BP = eukaryotic translation initiation factor 4E (eIF4E)-binding protein; AP = action potential; BFP = blue fluorescent protein; FCDII = focal cortical dysplasia type II; FMCD = focal malformation of cortical development; (c)GFP = (conditional) green fluorescent protein; IUE = *in utero* electroporation; mPFC = medial prefrontal cortex; mTOR(C1) = mechanistic target of rapamycin (complex 1); RMP = resting membrane potential; TSC = tuberous sclerosis complex; vEEG = video-EEG

Introduction

Hyperactivation of mechanistic target of rapamycin (mTOR) signalling causes a spectrum of neurodevelopmental disorders associated with focal malformation of cortical development (FMCD), including tuberous sclerosis complex (TSC), focal cortical dysplasia type II (FCDII) and hemimegalencephaly (HME).[1] These disorders result from germline or somatic mutations in mTOR complex 1 (mTORC1) pathway genes and are the most common causes for intractable epilepsy in children.[2–4] FMCDs in TSC, FCDII and HME share core histopathological features characterized by cortical mislamination, neuronal heterotopia and the presence of dysmorphic cytomegalic neurons with enhanced mTORC1 activation.[5] Numerous studies in mouse models of FMCD have shown that treatment with the mTORC1 inhibitor, rapamycin, prevents FMCD formation and reduces spontaneous seizures.[6,7] These findings emphasize the central role of mTORC1 dysregulation in the etiology of these disorders and the importance of identifying the mechanisms downstream of mTORC1 that lead to FMCD and epilepsy.

The mTORC1 pathway is a key regulator of cell growth that controls multiple cellular processes, including cap-dependent translation, autophagy, lysosome biogenesis and lipid synthesis, among others.[8,9] Hyperactive mTORC1 signalling is thought to alter neuron structure and function, leading to pro-epileptogenic circuit formation and epilepsy.[10] Despite the fact that numerous cellular processes are dysregulated under hyperactive mTORC1 conditions, it has been reported that correcting one of these functions, in particular cap-dependent translation, during foetal neurodevelopment is sufficient to reduce seizures in a mouse model of FMCD.[11] Consistent with this finding, normalizing translation before birth also rescued characteristic FMCD cytoarchitectural pathology, including neuronal misplacement, soma hypertrophy and dendrite and axon overgrowth.[11–13] Although these studies suggest that neuronal misplacement and dysmorphogenesis contribute to seizures, other neuronal alterations that promote epilepsy have been reported in FMCDs. In particular, we previously found that dysmorphic cytomegalic neurons in TSC and FCDII patients and FMCD pyramidal neurons (modelling human dysmorphic neurons) in mice display aberrant expression of hyperpolarization-activated cyclic nucleotide-gated isoform 4 (HCN4) channels.[14] The abnormal presence of these channels confers a unique mode of excitability in FMCD neurons that is dependent on intracellular cyclic adenosine monophosphate (cAMP) levels. Silencing HCN4 channel activity before birth prevented seizures in mice with FMCD, supporting their role in seizure generation. Further, the aberrant HCN4 channel expression was prevented by rapamycin treatment, suggesting that this is an mTORC1-dependent process. However, it is unknown whether normalizing cap-dependent translation can rescue aberrant HCN4 channel expression and restore neuron excitability. Importantly, it is unknown whether modifying dysregulated translation beyond the prenatal period, once FMCD is formed and epilepsy is established, can reverse neuronal alterations and alleviate seizures. Addressing these issues is crucial with regards to therapeutics because these neurodevelopmental disorders are predominantly diagnosed during infancy or childhood, when patients present with symptoms.[15–19]

Here, we investigated whether targeting aberrant translation once the mTORC1-induced developmental pathologies are established reverses neuronal dysfunction and spontaneous seizures in a mouse model of FMCD. mTORC1 promotes cap-dependent translation by directly phosphorylating and inactivating the translational repressor, eukaryotic translation initiation factor 4E (eIF4E)-binding protein (4E-BP). Phosphorylated 4E-BPs dissociate from eIF4E, allowing eIF4E to interact with other eukaryotic initiation factors to form the eIF4F complex and initiate translation.[20,21] mTORC1 hyperactivation thus leads to 4E-BP hyperphosphorylation and overactive translation due to decreased translational repression. Consistent with this, we found increased levels of phosphorylated 4E-BP1 in brain tissue from TSC and FCDII patients and from mice with FMCD. To compensate for the hyperphosphorylated 4E-BP1 in mice, we expressed a constitutively active form of 4E-BP1 (4E-BP1^{CA}; F113A mutation) which resists phosphorylation by mTORC1 and constitutively binds to eIF4E.[22,23] We performed timed expression of 4E-BP1^{CA} in FMCD neurons in juvenile animals by employing *in utero* electroporation (IUE) to target specific neuronal populations and tamoxifen-inducible conditional vectors to attain temporal control of gene expression. Subsequent neurophysiological analysis by patch clamp recording and videoEEG (vEEG) showed that 4E-BP1^{CA} expression corrected several electrophysiological alterations, including aberrant HCN4 channel expression, normalized cortical spectral activity and decreased seizures. Collectively, these findings support targeting 4E-BP-mediated translation as a strategy to treat epilepsy and underlying neuronal aberrancies in FMCDs.

Materials and methods

Human tissue samples

Resected brain (cortex) tissue samples were obtained from individuals who underwent epilepsy surgery at Texas Children's Hospital (Houston, TX, USA; one FCDII, two TSC) and Xiangya Hospital, Central South University (Changsha, China; two FCDII). One TSC sample was obtained from the Tuberous Sclerosis Complex Alliance. Patient pathological diagnosis, sex and age are listed in Table 1. Tissue collection and use were approved by the Institutional Review Boards at Baylor College of Medicine and Yale University School of Medicine and the human ethical committee at Xiangya Hospital, Central South University. All samples were obtained directly from the operating room. Samples for immunofluorescence staining were rapidly frozen in optimal cutting temperature compound and stored at –80°C until use. Frozen, unfixed tissue was cut into 15-μm thick sections using a cryostat and mounted onto microscope glass slides. Mounted sections were then fixed in ice-cold 4% paraformaldehyde for 5 min, followed by 3 × 5 min rinses in phosphate-buffered saline (PBS) immediately before immunofluorescence staining as described below. Samples for immunohistochemistry were fixed in 10% formalin and stored at room temperature until use. Fixed samples were cut into 3–5-μm

thick sections and stained using standard immunohistochemistry protocol.

Animals

All animal procedures were performed in accordance with Yale University Institutional Animal Care and Use Committee's regulations. Experiments were performed on male and female CD-1 mice (Charles River Laboratories).

Plasmid DNA

pCAG-Rheb^{CA} (also known as Rheb^{S16H}) was a gift from Dr Kentaro Hanada.[24] pCAG-TagBFP (BFP, blue fluorescent protein) was a gift from Dr Joshua Breunig.[25] pCAG-tdTomato (#83029) was previously generated in our laboratory[26] and is available through Addgene. pCALNL-GFP (cGFP, conditional green fluorescent protein, #13770), pCAG-ER^{T2}Cre-ER^{T2} (#13777) and pCAG-GFP (#11150) were obtained from Addgene. pCALNL-4E-BP1^{CA} (c4E-BP1^{CA}, conditional 4E-BP1^{CA}; also known as c4E-BP1^{F113A}) was generated by excising GFP from the pCALNL-GFP backbone through sequential digestion with EcoRI and NotI restriction enzymes and inserting the 4E-BP1^{CA} sequence from pCAG-4E-BP1^{CA} (Addgene #81122) between the EcoRI and NotI sites.

In utero electroporation

Timed-pregnant embryonic Day (E) 15.5 mice were anaesthetized with isoflurane and a midline laparotomy was performed to expose the uterine horns. A DNA plasmid solution (1.5 μl) was injected into the right lateral ventricle of each embryo using a glass pipette. For Fig. 1 and Supplementary Fig. 1B and C, a solution consisting of 2.5 μg/μl Rheb^{CA} (or BFP) + 1.0 μg/μl tdTomato was injected per embryo. For Supplementary Fig. 1D and E, 3.5 μg/μl Rheb^{CA} (or tdTomato) + 1.0 μg/μl GFP was injected per embryo. For Figs 2–5, 3.0 μg/μl c4E-BP1^{CA} (or cGFP) + 2.5 μg/μl Rheb^{CA} + 0.4 μg/μl ER^{T2}Cre-ER^{T} + 0.8 μg/μl tdTomato was injected per embryo. For each litter, half of the embryos were injected with the experimental condition and the other half received the respective control condition. Figure 2 also included a littermate control group that received 2.5 μg/μl BFP + 0.8 μg/μl tdTomato + 0.4 μg/μl ER^{T2}Cre-ER^{T2} + 3.0 μg/μl cGFP per embryo. All plasmid solutions were diluted in water and contained 0.03% Fast Green dye to visualize the injection. A 5-mm tweezer electrode was positioned on the embryo head and 6 × 42 V, 50-ms pulses at 950-ms intervals were applied using a pulse generator (ECM830, BTX) to electroporate the plasmids into neural progenitor cells. Electrodes were positioned to target expression in the medial prefrontal cortex (mPFC). The embryos were returned to the abdominal cavity and allowed to continue with development.

Tamoxifen administration

Tamoxifen (Cayman Chemical #13258) was dissolved in corn oil (Sigma) at a stock concentration of 10 mg/ml and stored at 4°C, protected from light. Tamoxifen was prepared fresh prior to each experiment. Mice were administered tamoxifen via intraperitoneal injections at a dose of 75 mg/kg once daily for 5 days. Mice were injected from postnatal Day (P) 12 to P16 for patch clamp recording (Fig. 2) and P28 to P32 for histology and EEG recording (Figs 3–5). Control groups receiving vehicle were included.

Brain tissue fixation and immunofluorescence staining

Mice were deeply anaesthetized with sodium pentobarbital (85 mg/kg intraperitoneal injection) and perfused with ice-cold PBS followed by 4% paraformaldehyde. Whole brains were dissected and post-fixed in 4% paraformaldehyde for 2 h and then cryoprotected in 30% sucrose for 24–48 h at 4°C until they sank to the bottom of the tubes. Brains were serially cut into 50-μm thick coronal sections using a freezing microtome and stored in PBS + 0.01% sodium azide at 4°C until use.

For immunofluorescence staining, human (mounted) and mouse (free-floating) tissue sections were washed in PBS + 0.1% Triton X-100 (PBS-T) for 2 × 10 min and permeabilized in PBS + 0.3% Triton X-100 for 20–30 min. Sections were then incubated in blocking buffer (10% normal goat serum + 0.3% bovine serum albumin + 0.3% Triton X-100 in PBS) for 1–2 h at room temperature. Mounted human tissue sections were incubated in primary antibodies (diluted in 5% normal goat serum + 0.3% bovine serum albumin + 0.1% Triton X-100 in PBS) for 1 day in a humidity chamber at room temperature. Free-floating mouse tissue sections were incubated in primary antibodies for 2 days at 4°C. Following primary antibody incubation, sections were washed in PBS-T for 3 × 10 min and incubated in secondary antibodies for 2 h at room temperature. Sections were then incubated in DAPI for 10 min, washed in PBS-T for 3 × 30 min and rinsed in PBS before they were mounted onto microscope glass slides and coverslipped.

Antibodies

The following primary antibodies were used: SMI-311 (BioLegend #837801, 1:200), phosphorylated (p)-4E-BP1 Thr37/46 (Cell Signaling Technology #2855, 1:200 for immunofluorescence, 1:300 for immunohistochemistry), p-4E-BP1/2/3 Thr45 (Bioss Antibodies bs-6421R, 1:200–1:500), HCN4 (Alomone Labs APC-052, 1:500), HCN1 (APC-056, 1:500), HCN2 (APC-030, 1:500) and HCN3 (APC-057, 1:500). The following secondary antibodies were used: goat anti-mouse IgG Alexa Fluor Plus 488 (Invitrogen A#32723), anti-rabbit IgG Alexa Fluor Plus 594 (A#32740) and anti-rabbit IgG Alexa Fluor Plus 647 (#A32733) (all 1:500).

Microscopy and image analysis

Images were acquired using Zeiss LSM 880 or Olympus Fluoview FV1000 confocal microscopes. Tile scan images were stitched together using Zeiss Zen Blue software. All image analyses were done using ImageJ software (National Institutes of Health) and were performed blinded to experimental groups. Data were quantified using greyscale images of single optical sections unless noted otherwise. Representative images were prepared using Adobe Photoshop CC. All images meant for direct comparison were taken with the same microscope settings and uniformly processed.

For Fig. 1, cell size was quantified by tracing the soma of tdTomato+ cells and measuring the area. p-4E-BP1 staining

Table 1 Patient information for TSC and FCDII tissue samples

Subject ID	Pathological diagnosis	Sex	Age
TSC (#1)	TSC	Unknown	Unknown
TSC (#2)	TSC	Female	4 years
TSC (#3)	TSC	Female	2 years
FCDII (#1)	FCDII	Male	7 years
FCDII (#2)	FCDII	Female	13 years
FCDII (#3)	FCDII	Female	5 years

intensity was quantified by measuring the mean grey value within the same traced cells. For Supplementary Fig. 1, p-4E-BP1/2/3 staining intensity was quantified by measuring the mean grey value within tdTomato+ or GFP+ cells. For each animal, 22–30 (Fig. 1) or 12 (Supplementary Fig. 1) randomly selected cells from two brain sections were measured; each data-point represents averaged values per animal. Staining intensities were normalized to the respective mean control. For Fig. 3 and Supplementary Fig. 4, cell size was quantified by tracing the soma of tdTomato+ cells and measuring the area. Cell size was analysed from maximum intensity projection images created from a 20-μm thick z-stack of optical sections taken at 2 μm increments. For each animal, 50 randomly selected tdTomato+ cells from three brain sections were measured; each data-point represents averaged values per animal. Cell placement was quantified by counting all tdTomato+ cells within an 850 μm × 850 μm region of interest surrounding the electroporated cortex. Cells within 300 μm from the pial surface were considered correctly located in layer (L) 2/3 whereas cells outside that boundary were considered misplaced. For each animal, three brain sections were analysed; each data-point represents averaged values per animal. Data are shown as percent of total counted tdTomato+ cells. For Fig. 3 and Supplementary Fig. 5, HCN1–4 staining intensity was quantified using images containing both the ipsilateral (electroporated) and contralateral cortices within the same plane of view. For each brain section, the mean grey value was measured in three randomly selected, non-overlapping 200 × 200 μm regions of interest within the electroporated area and in three position-matched regions of interest on the non-electroporated contralateral side. We analysed two brain sections per animal for HCN4 and one brain section per animal for HCN1–3; each data-point represents averaged values from six (or three) regions of interest per animal. Staining intensities were normalized to the respective mean control ($Rheb^{CA}$ + cGFP contralateral cortex).

Acute slice preparation and whole-cell patch clamp recording

P23–32 mice were deeply anaesthetized with isoflurane. Whole brains were rapidly dissected and immersed in ice-cold oxygenated (95% O_2/5% CO_2) high-sucrose cutting solution (in mM: 213 sucrose, 2.6 KCl, 1.25 NaH_2PO_4, 3 $MgSO_4$, 26 $NaHCO_3$, 10 dextrose, 1 $CaCl_2$, 0.4 ascorbate, 4 Na-lactate, 2 Na-pyruvate, pH 7.4 with NaOH). Acute brain slices 300-μm thick containing the mPFC were cut using a vibratome (Leica VT1000). Slices were allowed to recover in a holding chamber with oxygenated artificialCSF (in mM: 118 NaCl, 3 KCl, 1.25 NaH_2PO_4, 1 $MgSO_4$, 26 $NaHCO_3$, 10 dextrose, 2 $CaCl_2$, 0.4 ascorbate, 4 Na-lactate, 2 Na-pyruvate, 300 mOsm/kg, pH 7.4 with NaOH) at 32°C for 45 min before returning to room temperature (25°C) where they were kept for 6–8 h during the experiment.

Whole-cell current clamp and voltage clamp recordings were performed in a recording chamber at 28°C, using pulled borosilicate glass pipettes (4–7 MΩ resistance, Sutter Instrument) filled with an internal solution (in mM: 125 K-gluconate, 4 KCl, 10 HEPES, 1 EGTA, 0.2 $CaCl_2$, 10 di-tris-phosphocreatine, 4 Mg-ATP, 0.3 Na-GTP, 280 mOsm/kg, pH 7.3 with KOH). Fluorescent (electroporated) neurons in the mPFC were visualized using epifluorescence on an Olympus BX51WI microscope with a 40× water immersion objective. Recordings were acquired from L2/3 using an Axopatch 200B amplifier and pClamp software (Molecular Devices). Data were filtered at 5 kHz and digitized with Digidata 1320 (Molecular Devices).

The resting membrane potential (RMP) was recorded within the first 10 s after achieving whole-cell configuration in current clamp mode while the cell was at rest without any current injection. The membrane capacitance and I_h were measured in voltage clamp mode. The membrane capacitance was calculated by dividing the average membrane time constant by the average input resistance obtained from the current response to a 500-ms long, ± 5 mV voltage step from –70 mV holding potential. I_h was activated by a 1-s long conditioning step to –40 mV from a holding potential of –70 mV, followed by a series of 3-s long hyperpolarizing voltage steps from –130 mV to –40 mV in 10-mV increments. I_h amplitudes (ΔI) were measured as the difference between the instantaneous current immediately following each test potential (I_{inst}) and the steady-state current at the end of each test potential (I_{ss}).[27,28] The voltage sag, resting membrane conductance and action potential (AP) properties were measured in current clamp mode. The voltage sag was evoked by a series of 1-s long hyperpolarizing currents from –500 pA to 0 pA in 100-pA increments from rest. The amplitude of the voltage sag in response to the –500-pA hyperpolarizing current step (sag ratio) was quantified using the equation $(V_{peak} - V_{ss})/V_{peak} \times 100$, where V_{peak} is the maximum voltage deflection and V_{ss} is the steady-state voltage at the end of the hyperpolarizing pulse.[27,29] The resting membrane conductance was calculated using the membrane potential change evoked by the –500-pA hyperpolarizing current step. The AP input–output curve was generated by injecting 500-ms long depolarizing currents steps from 0 to 1000 pA in 50-pA increments. Only values from 0 to 700 pA were plotted due to the inactivation of sodium channels in control neurons at >700 pA injections. The AP threshold, peak amplitude and half-width were analysed from averaged traces of 5–10 consecutive APs induced by a 50-ms long minimal current (needed to induce the first AP) + 10 pA. The AP threshold was defined as the membrane potential at which the first derivative of an evoked AP achieved 10% of its peak velocity (dV/dt). The AP peak amplitude was defined as the difference between the peak and baseline. The AP half-width was defined as the duration of the AP at the voltage halfway between the peak and baseline. The first and ninth interspike intervals were calculated by measuring the time between the peaks of the first and second spike and the ninth and 10th spike, respectively, using the first obtained trace with ⩾10 spikes. All data analysis was performed offline using pClamp software and exported to GraphPad Prism 9 software for graphing and statistical analysis.

Video-EEG recording and analysis

Electrode implantation

Mice were implanted with prefabricated EEG headmounts (Pinnacle Technology, Inc. #8201-EEG) at 9–11 weeks of age. Mice were anaesthetized with isoflurane and positioned on a stereotaxic frame using ear bars. A rostro-caudal midline incision was made in the skin to expose the skull surface. Four pilot holes (two bilateral holes 1 mm anterior to bregma and two bilateral holes 5 mm posterior to bregma, each 1.5 mm lateral to the sagittal suture) were tapped through the skull to the dura mater using a 23-gauge needle to accommodate the EEG headmount. The headmount was attached on top of the skull with superglue and four stainless steel screws (Pinnacle Technology, cat. no. 8209) were threaded into the pilot holes. Silver conductive paint was applied around the screw threads to ensure a solid connection with the headmount. The entire implant was insulated using dental acrylic. Mice were allowed to recover in their home cage for at least 5 days before vEEG recording.

Video-EEG recording

Mice were vEEG-recorded starting at 10–13 weeks of age, during which they were housed in individual recording chambers in a

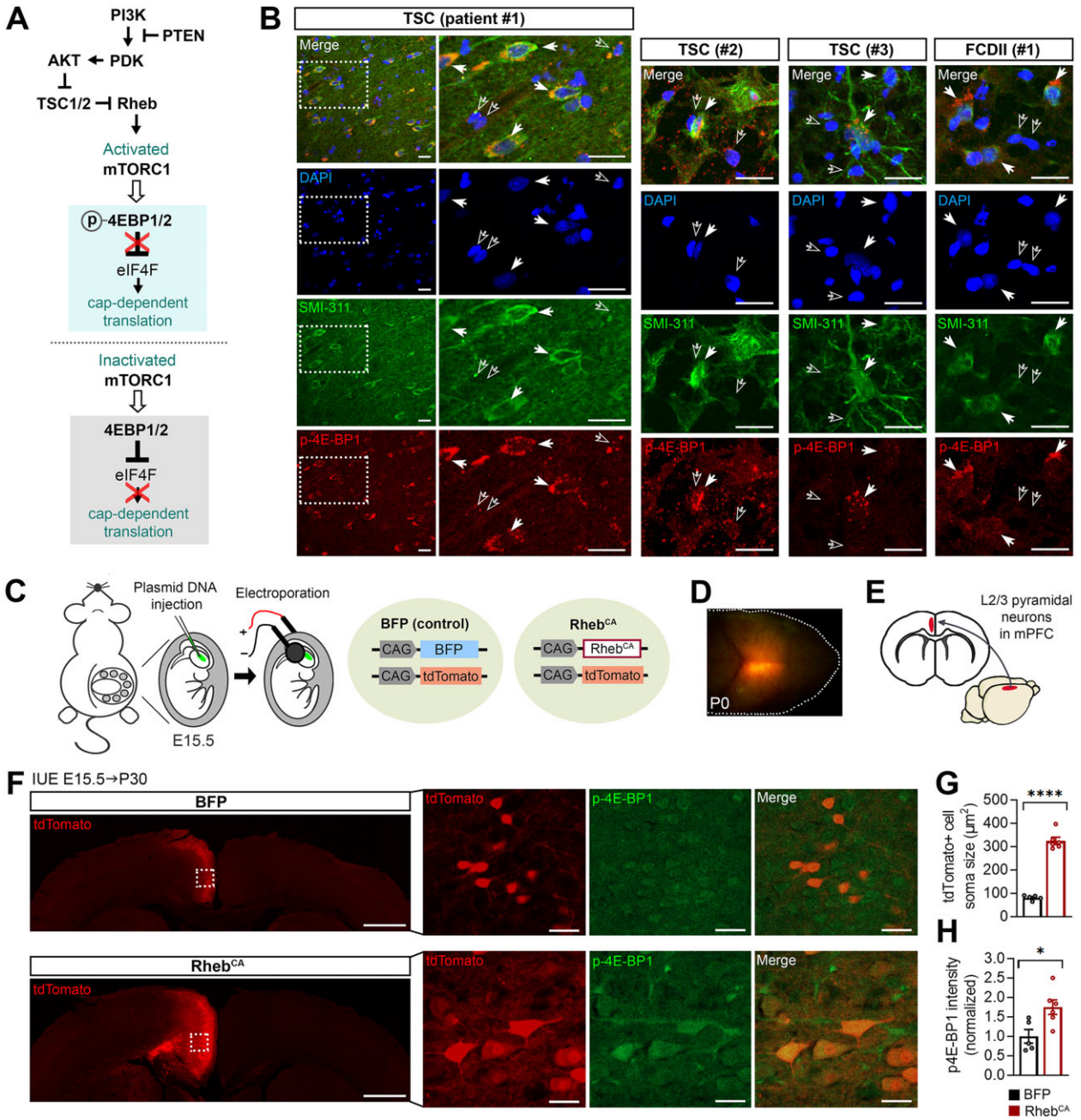

Figure 1 4E-BP1 is hyperphosphorylated in human FMCD tissue and in the Rheb^{CA} mouse model of FMCD. (**A**) Diagram of the PI3K-mTORC1 pathway and downstream regulation of cap-dependent translation via 4E-BP1/2. Activated mTORC1 phosphorylates and inhibits 4E-BP1/2, which disinhibits the eIF4F complex (via release of eIF4E) and promotes cap-dependent translation. Conversely, inactivated mTORC1 disinhibits 4E-BP1/2, which inhibits 4E-BP1/2 and blocks cap-dependent translation. (**B**) Representative images of DAPI (blue), SMI-311 (green) and p-4E-BP1 (red) staining in resected brain tissue samples from three individuals with TSC and one individual with FCDII who underwent epilepsy surgery. For Individual TSC #1, low-magnification images are shown on the *left* and high-magnification images are shown on the *right*. White squares denote the magnified areas. For all images, filled arrows point to SMI-311+ dysmorphic neurons with high p-4E-BP1 immunoreactivity. Unfilled arrows point to surrounding SMI-311– cells with low or no p-4E-BP1 immunoreactivity. Note that DAPI-stained nuclei in SMI-311+ cells appear fainter and are often enlarged compared to SMI-311– cells. Scale bars = 25 μm. (**C**) Diagram of IUE and plasmids used to generate Rheb^{CA} mice with FMCD. Mouse embryos were electroporated with a BFP (control) or Rheb^{CA} plasmid at E15.5, targeting radial glia generating pyramidal neurons destined to L2/3 in the mPFC. tdTomato was co-electroporated in both conditions to label the targeted neurons. (**D**) Image of a P0 pup head showing tdTomato fluorescence in the targeted region following electroporation at E15.5. (**E**) Diagram showing the targeted region (red) in an adult mouse brain and the corresponding area in coronal view. (**F**) Representative images of tdTomato+ cells (red) and p-4E-BP1 staining (green, pseudocoloured) in coronal cortical sections from P30 BFP control and Rheb^{CA} mice. Low-magnification tile scan images of tdTomato+ cells are shown on the *left*. tdTomato+ cells are strictly found in L2/3 in BFP control mice and misplaced across the cortical layers in Rheb^{CA} mice. High-magnification images of tdTomato+ cells and p-4E-BP1 staining are shown on the *right*. tdTomato+ cells display basal level p-4E-BP1 immunoreactivity in BFP control mice and high p-4E-BP1 immunoreactivity in Rheb^{CA} mice. White squares denote the magnified areas. Scale bars = 1000 μm (*left*), 25 μm (*right*). (**G**) Quantification of tdTomato+ cell soma size. $n = 5$ BFP, $n = 6$ Rheb^{CA} mice; each data-point represents averaged values from 22 to 30 cells per animal. Data were analysed by unpaired *t*-test; $^{****}P < 0.0001$. (**H**) Quantification of p-4E-BP1 intensity in tdTomato+ cells. $n = 5$ BFP, $n = 6$ Rheb^{CA} mice; each data-point represents averaged values from 22 to 30 cells per animal. Data were normalized to the mean control (BFP) and analysed by unpaired *t*-test; $^{*}P = 0.0186$. Error bars are ± SEM.

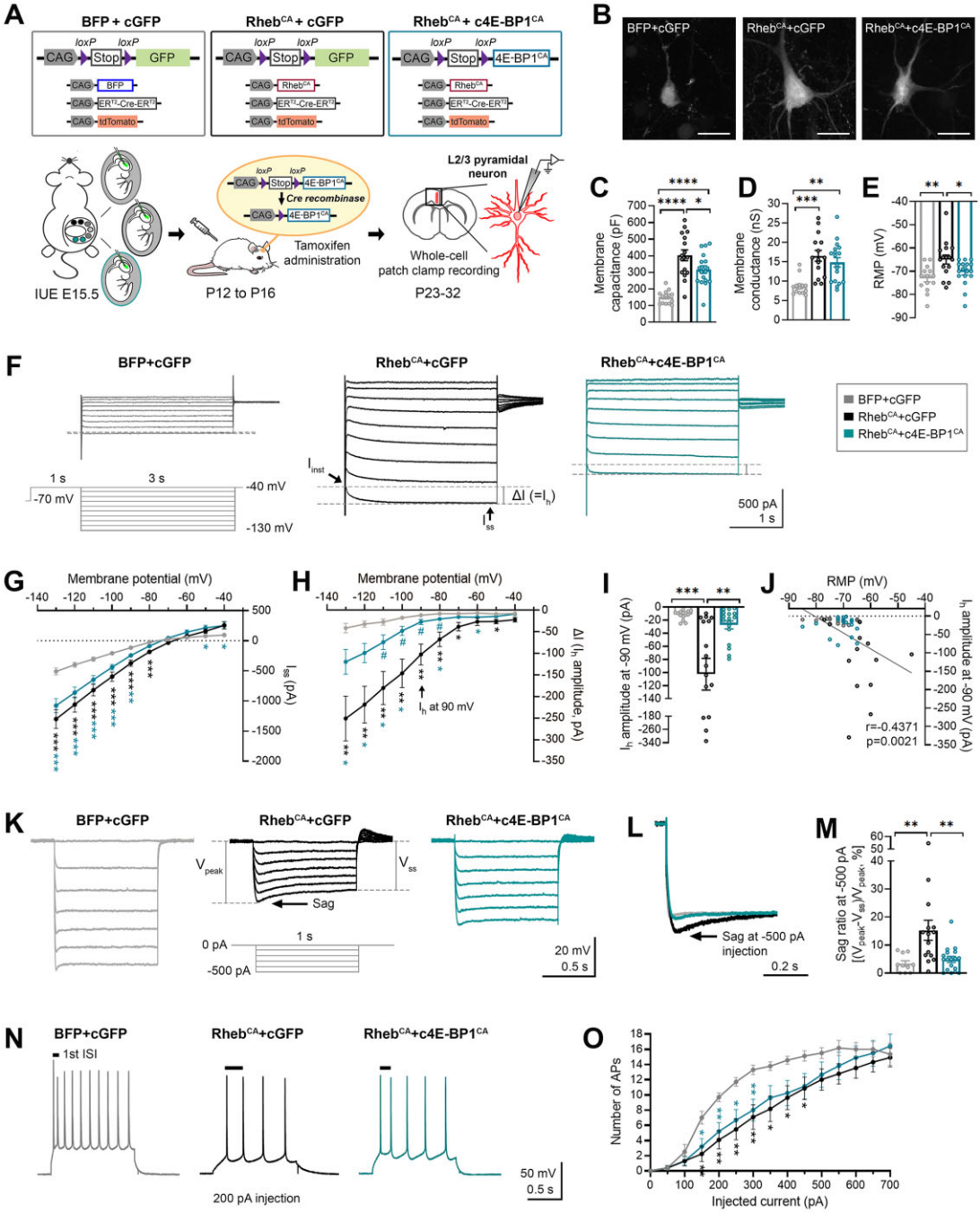

Figure 2 Juvenile expression of c4E-BP1^{CA} restores the excitability of Rheb^{CA} neurons. (**A**) Diagram of plasmids used to generate BFP + cGFP (control), Rheb^{CA} + cGFP and Rheb^{CA} + c4E-BP1^{CA} mice and experimental strategy. Mouse embryos were electroporated at E15.5. For each litter, 1/3 of the embryos received BFP + cGFP, 1/3 received Rheb^{CA} + cGFP and 1/3 received Rheb^{CA} + c4E-BP1^{CA} plasmids. A tamoxifen-inducible Cre (ER^{T2}-Cre-ER^{T2}) plasmid and a tdTomato reporter plasmid were co-electroporated in all three conditions. Tamoxifen was administered to all mice from P12 to P16 to induce GFP or 4E-BP1^{CA} expression. Whole-cell patch clamp recordings were performed in L2/3 pyramidal neurons in acute coronal slices from P23–32 mice. (**B**) Representative images of tdTomato + (electroporated) neurons from brain slices used in patch clamp recording. Images are maximal intensity projections of 25-μm thick z-stack sections. Scale bars = 20 μm. (**C–E**) Bar graphs of (**C**) membrane capacitance, (**D**) resting membrane conductance and (**E**) RMP. (**F**) Representative current traces in response to a 1-s long conditioning step to –40 mV from a holding potential of –70 mV, followed by a series of 3-s long hyperpolarizing voltage steps from –130 mV to –40 mV in 10-mV increments. Traces at the –40 mV conditioning step are not shown due to overlapping traces from unclamped sodium spikes. (**G**) IV curve obtained from I_{ss} amplitudes. (**H**) IV curve obtained from I_h amplitudes or ΔI, where $\Delta I = I_{ss} - I_{inst}$. (**I**) Quantification of I_h amplitude at –90 mV. (**J**) Scatterplot of I_h amplitudes at –90 mV versus RMP. $n = 47$ XY pairs. $P = 0.0021$ by Pearson product–moment correlation. (**K**) Representative voltage traces in response to 1-s long hyperpolarizing current steps from –500 pA to 0 pA in 100-pA increments from RMP. Arrow points I_h-associated voltage sags induced by hyperpolarizing currents. (**L**) Representative voltage traces in response to –500 pA current steps. Traces were rescaled and superimposed post-recording to visualize the differences in voltage sag size between groups. (**M**) Quantification of voltage sag ratio at –500 pA, where sag ratio = $(V_{peak} - V_{ss})/V_{peak} \times 100$. (**N**) Representative traces of AP firing response to depolarizing current injections. (**O**) Input–output curve showing the mean number of APs fired in response to 500-ms long depolarizing current steps from 0 to 700 pA in 50-pA increments. For all graphs, n = 10–14 BFP + cGFP, n = 13–16 Rheb^{CA} + cGFP, n = 17–18 Rheb^{CA} + c4E-BP1^{CA} neurons. Data were analysed using (**C–E, I** and **M**) one-way ANOVA with Tukey's *post hoc* test; $^{*}P < 0.05$, $^{**}P < 0.01$, $^{***}P < 0.001$, $^{****}P < 0.0001$ or (**G, H** and **O**) mixed-effects ANOVA with Tukey's *post hoc* test; $^{*}P < 0.05$, $^{**}P < 0.01$, $^{***}P < 0.001$ (versus BFP + cGFP), $^{\#}P < 0.05$ (versus Rheb^{CA} + cGFP). Error bars are ± SEM.

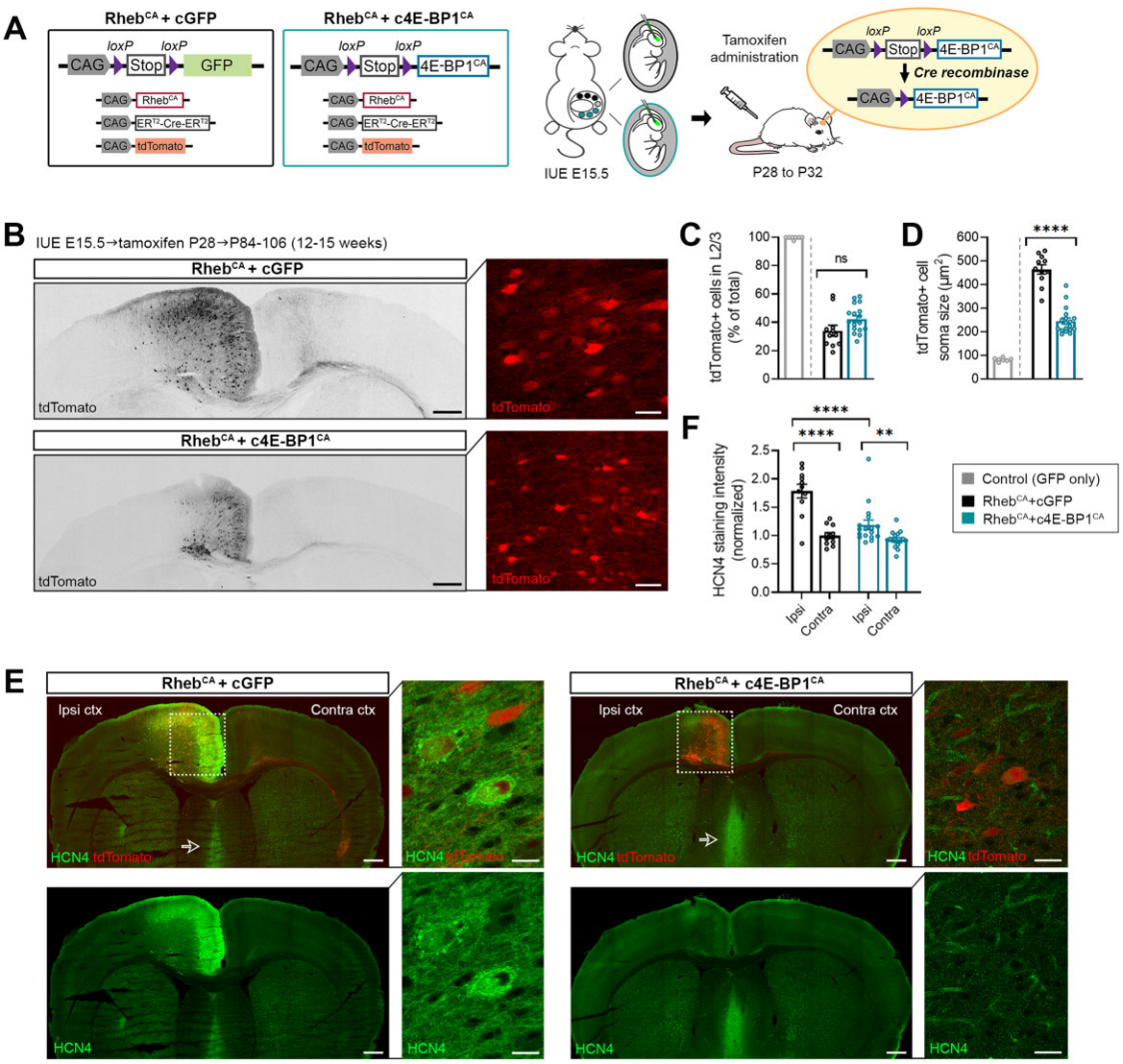

Figure 3 c4E-BP1^{CA} expression in juvenile Rheb^{CA} mice reduces neuronal cytomegaly and aberrant HCN4 channel expression. (**A**) Diagram of plasmids used to generate Rheb^{CA} + cGFP and Rheb^{CA} + c4E-BP1^{CA} mice and experimental strategy. Mouse embryos were electroporated at E15.5. For each litter, half of the embryos received Rheb^{CA} + cGFP and the other half received Rheb^{CA} + c4E-BP1^{CA}. A tamoxifen-inducible Cre (ER^{T2}-Cre-ER^{T2}) plasmid and a tdTomato reporter plasmid were co-electroporated in both conditions. Tamoxifen was administered from P28 to P32 to induce GFP or 4E-BP1^{CA} expression. (**B**) Representative images of tdTomato + cells in coronal sections from P84–106 Rheb^{CA} + cGFP and Rheb^{CA} + c4E-BP1^{CA} mice. Low-magnification tile scan images showing tdTomato + cell distribution across the cortical layers are on the *left*. High-magnification images showing differences in tdTomato + cell size are on the *right*. Scale bars = 500 μm (*left*), 50 μm (*right*). (**C**) Quantification of tdTomato + cell placement in L2/3. $n = 11$ Rheb^{CA} + cGFP, 18 Rheb^{CA} + c4E-BP1^{CA} mice; each data-point represents averaged values from three brain sections per animal. Data were analysed by unpaired *t*-test. (**D**) Quantification of tdTomato + cell soma size. $n = 11$ Rheb^{CA} + cGFP, $n = 18$ Rheb^{CA} + c4E-BP1^{CA} mice; each data-point represents averaged values from 50 cells per animal. Data were analysed by unpaired *t*-test; $^{****}P < 0.0001$. For graphs **C** and **D**, previously reported levels for age-matched control mice electroporated with GPF only (Nguyen *et al.*[30]) are shown for comparison. (**E**) Representative images of tdTomato + cells (red) and HCN4 staining (green, pseudocoloured) in coronal sections from P84–106 Rheb^{CA} + cGFP and Rheb^{CA} + c4E-BP1^{CA} mice. Low-magnification tile scan images showing HCN4 staining in whole-brain sections are on the *left*. High-magnification images showing somatic HCN4 staining in Rheb^{CA} + cGFP neurons and lack of HCN4 staining in Rheb^{CA} + c4E-BP1^{CA} neurons are on the *right*. White squares denote the areas targeted by IUE. Arrows point to HCN4 staining in the medial septum. Scale bars = 500 μm (*left*), 25 μm (*right*). (**F**) Quantification of HCN4 staining intensity. $n = 11$ Rheb^{CA} + cGFP, $n = 17$ Rheb^{CA} + c4E-BP1^{CA} mice; each data-point represents averaged values from two brain sections per animal. Data were normalized to the mean control (Rheb^{CA} + cGFP contralateral cortex) and analysed using two-way repeated measures ANOVA with Bonferroni's *post hoc* test; $^{**}P < 0.01$, $^{****}P < 0.0001$. Error bars are ± SEM. Ipsi ctx = ipsilateral cortex; contra ctx = contralateral cortex.

light-, temperature- and humidity-controlled room with *ad libitum* access to food and water. Synchronous vEEG recording was acquired using a tethered three-channel EEG system (Pinnacle Technology, Inc. #8200-K1-iSE3) and Sirenia Acquisition software (Pinnacle Technology, Inc.). EEG data were acquired at a 400-Hz sampling rate and 1.0-Hz high-pass filtering. Mice were recorded 24 h/day for at least 7 consecutive days. The average recording hours per animal was 179.8 ± 16.7 (± SD) h.

Seizure analysis

Seizure frequency was analysed using Sirenia Seizure Basic software (Pinnacle Technology, Inc.). All analyses were performed blinded to experimental groups. The entire EEG traces were manually reviewed for the occurrence of seizures, defined as a sudden onset of high-amplitude activity with a characteristic pattern of progressive frequency and amplitude increases over the course of

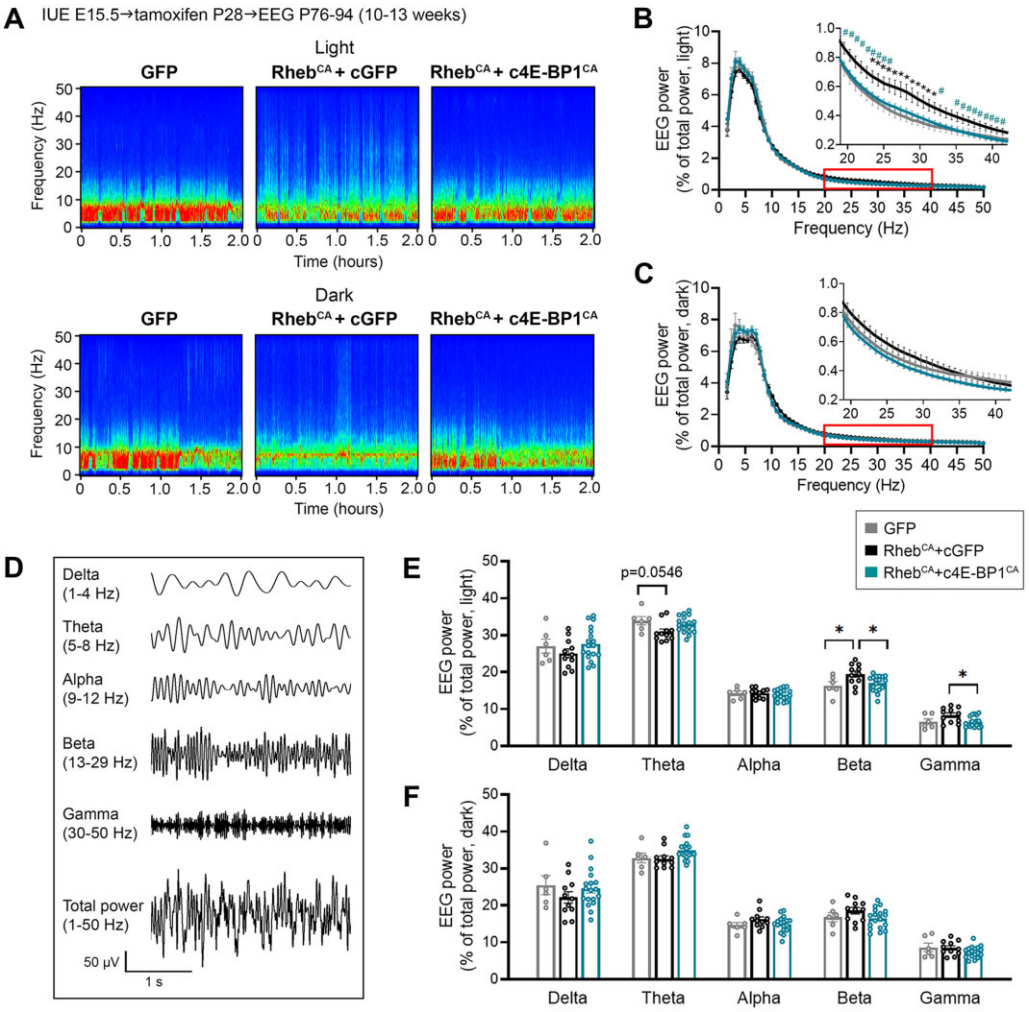

Figure 4 c4E-BP1^{CA} expression after epilepsy onset in juvenile Rheb^{CA} mice normalizes cortical spectral activity. (**A**) Representative spectrograms of background EEG during the light (12–2 p.m., *top*) and dark (12–2 a.m., *bottom*) cycles. (**B** and **C**) Relative EEG power spectra of background EEG during the (**B**) light and (**C**) dark cycles. *Insets* show enlarged graphs from the areas denoted by the red boxes. (**D**) Sample cortical EEG traces showing the delta, theta, alpha, beta and gamma frequency bands. The bands were decomposed from the composite EEG signal shown at the bottom. (**E** and **F**) Bar graphs of the delta, theta, alpha, beta and gamma relative bandpower during the (**E**) light and (**F**) dark cycles. For all graphs, $n = 6$ GFP, $n = 11$ Rheb^{CA} + cGFP, $n = 18$ Rheb^{CA} + c4E-BP1^{CA} mice; each data-point represents averaged values from 3 to 10 cycles (epochs) per animal. Data were analysed using (**B** and **C**) two-way repeated measures ANOVA with Tukey's *post hoc* test; $^{*}P < 0.05$ (versus GFP), $^{\#}P < 0.05$ (versus Rheb^{CA} + cGFP) or (**E** and **F**) one-way ANOVA with Tukey's *post hoc* test; $^{*}P < 0.05$. Error bars are ± SEM.

the event lasting ⩾10 s.[30] Video data were visually inspected for behavioural correlates, including myoclonic jerks, tonic–clonic activity, convulsions and loss of postural control (rearing and falling), and were used as secondary verification of seizures. The mean number of seizures per day (seizures/day) was obtained by dividing the total number of seizures by total recording hours and multiplied by 24 for each animal. The proportion of mice with 0, <1, or >1 seizures/day was determined by dividing the number of animals within the respective categories by the total number of animals for each group.

Spectral power analysis

Spectral power analysis of background EEG data was performed using LabChart v8 (AD Instruments). In addition to the traces obtained from the Rheb^{CA} + cGFP and Rheb^{CA} + c4E-BP1^{CA} mice, we analysed traces from six control mice that were electroporated with GFP only, which were acquired as part of a previous study.[30] EEG data from these animals were acquired under the same conditions, settings and age. For each animal, a 2-h epoch during each of the light (12–2 pm) and dark (12–2 am) cycles were analysed. Any seizures or artefacts within these epochs were removed prior to analysis. EEG data were converted into frequency components using fast Fourier transformation (FFT) with an FFT size of 512 and a Hann (cosine-bell) window with 50% overlap. Relative power spectra were obtained by dividing power values within each frequency bin by total power. Relative bandpower in the delta δ (1–4 Hz), theta θ (5–8 Hz), alpha α (9–12 Hz), beta β (13–29 Hz) and gamma γ (30–50 Hz) bands were calculated by dividing the sum of power within each frequency range by total power (1–50 Hz). Data from time-of-day-matched epochs over multiple days were averaged for each animal (3–5 epochs for GFP mice, 5–10 epochs for Rheb^{CA} + cGFP and Rheb^{CA} + c4E-BP1^{CA} mice per light/dark cycle). Data are shown as relative power to reduce individual animal variability stemming from headcap implantation.

Statistical analysis

Statistical analyses were performed using GraphPad Prism 9 software. The significance level was set at $P < 0.05$. The specific tests

that were used, test results and sample size (*n*, number of animals or neurons) are summarized in Supplementary Tables 1 and 2 and described in the figure legends. Data are presented as mean ± SEM.

Study design

We performed histological examination in resected human brain tissue and controlled laboratory experiments in mice. Human tissue samples from three individuals with TSC and three individuals with FCDII were evaluated for p-4E-BP1 staining intensity. Tissue from five (three male, two female) control mice and six (four male, two female) mice expressing constitutively active Rheb ($Rheb^{CA}$) were analysed for p-4E-BP1 and p-4E-BP1/2/3 intensity at P30. 3 (two male, one female) control and three (two male, one female) $Rheb^{CA}$ mice were analysed for p-4E-BP1/2/3 intensity at P165. For patch clamp recording, 14 BFP + cGFP, 16 $Rheb^{CA}$ + cGFP and 18 $Rheb^{CA}$ + c4E-$BP1^{CA}$ neurons randomly selected from three (one male, two female) BFP + cGFP, five (three male, two female) $Rheb^{CA}$ + cGFP and four (female) $Rheb^{CA}$ + c4E-$BP1^{CA}$ mice that received tamoxifen from P12 to P16, respectively, were recorded. The specific number of recorded cells for each parameter is indicated in Supplementary Tables 1 and 2 and the figure legends. The average age of recording was P26.8 ± 3.2 (± SD, range: 23–32). For histology and vEEG studies, 11 (six male, five female) $Rheb^{CA}$ + cGFP and 18 (10 male, eight female) $Rheb^{CA}$ + c4E-$BP1^{CA}$ mice that received tamoxifen from P28 to P32, as well as three (two male, one female) vehicle-treated $Rheb^{CA}$ + c4E-$BP1^{CA}$ (littermate with six of the tamoxifen-treated $Rheb^{CA}$ + c4E-$BP1^{CA}$) were evaluated. No sex differences in cell size, cell placement, HCN4 staining intensity, or seizure frequency were found in the $Rheb^{CA}$ + cGFP (Mann–Whitney U-test, $P < 0.05$ for all parameters) or $Rheb^{CA}$ + c4E-$BP1^{CA}$ ($P < 0.05$) groups, and data for males and females were therefore combined. The animals underwent vEEG recording first and brain tissue was collected afterward for histological examination. The average age of EEG recording start was 12.0 ± 1.0 weeks (± SD, range: 10.9–13.4 weeks) and the average age of tissue collection was 13.6 ± 1.3 weeks (± SD, range: 12.0–15.1 weeks). EEG data acquisition and analysis were performed completely blinded to experimental groups as animal identity and group could only be determined afterward by evaluating fluorescence markers on prepared brain sections. Data for EEG, cell size, cell placement and HCN4 (as well as HCN1–3) staining were from the same set of animals and are correlated in Fig. 5E–G. One $Rheb^{CA}$ + c4E-$BP1^{CA}$ mouse was excluded from HCN4 staining analysis because the hemispheres were split during tissue collection and it was not possible to analyse the ipsi- and contralateral sides within the same field of view. All data collection and analysis were performed blinded to experimental groups. Multiple independent IUEs were performed for each experiment, and littermate controls were included for all experiments.

Data availability

Data supporting the findings of this study are available within the article and its Supplementary material. Raw data are available upon reasonable request.

Results

4E-BP1 is hyperphosphorylated in human FMCD tissue and in the $Rheb^{CA}$ mouse model of FMCD

Activated mTORC1 phosphorylates and inhibits 4E-BP repressor activity to promote cap-dependent translation and, conversely, inactivated mTORC1 leads to dephosphorylated 4E-BPs and repressed translation (Fig. 1A).[20,21] To determine the phosphorylation states of 4E-BPs in human FMCD, we performed immunofluorescence staining for p-4E-BP1 in resected FMCD tissue samples from individuals with TSC or FCDII who underwent epilepsy surgery. We co-stained with the neurofilament marker SMI-311 to identify the dysmorphic cytomegalic neurons. These neurons have an abnormal cytoplasmic accumulation of neurofilament proteins that result in an intense neurofilament labelling.[31–33] We found marked p-4E-BP1 immunoreactivity in SMI-311+ dysmorphic neurons, whereas low or no p-4E-BP1 immunoreactivity was detected in surrounding SMI-311– cells in all samples (Fig. 1B). Increased p-4E-BP1 immunoreactivity was also observed in additional FCDII samples by immunohistochemical staining (Supplementary Fig. 1A). These results demonstrate the occurrence of 4E-BP1 hyperphosphorylation in human FMCD dysmorphic neurons and suggest the presence of overactive translation in these cells.

To model FMCD in mice, we expressed a constitutively active form of the canonical mTORC1 activator, Rheb ($Rheb^{CA}$), in developing mouse embryos using IUE, as previously described.[13,14,30,34,35] Mice were electroporated with plasmids encoding for $Rheb^{CA}$ or BFP (control) at E15.5, targeting radial glia that generate pyramidal neurons destined to L2/3 in the mPFC. A tdTomato reporter plasmid was co-electroporated in both conditions to label the targeted neurons (Fig. 1C–E). Histological examination was performed in juvenile mice at P30. Consistent with previous findings,[13,30,34,35] $Rheb^{CA}$ expression resulted in neuron misplacement across the cortical layers (Fig. 1F) and increased neuron soma size (Fig. 1F and G and Supplementary Table 1). Immunostaining for p-4E-BP1 revealed significantly increased p-4E-BP1 levels in $Rheb^{CA}$ neurons compared to control neurons (Fig. 1F and H, Supplementary Table 1). Similar results were also found when stained with a p-4E-BP1/2/3 antibody that recognizes all 4E-BP isoforms at P30 and P165 (Supplementary Fig. 1B–E and Supplementary Table 2). Thus, dysregulation of 4E-BP1 occurs in both human and mouse FMCD.

Juvenile expression of c4E-$BP1^{CA}$ restores the excitability of $Rheb^{CA}$ neurons

To elucidate the contribution of 4E-BP to mTORC1-induced neuronal alterations, we first examined whether compensating for the dysregulated 4E-BP1 activity by expressing 4E-$BP1^{CA}$ would rescue $Rheb^{CA}$ neuron function. Previously, we showed that co-expressing $Rheb^{CA}$ and 4E-$BP1^{CA}$ during embryonic development in mice prevented neuron misplacement, significantly reduced neuron overgrowth and rescued the RMP.[13] Considering that FMCD-related epilepsies are diagnosed after birth and most therapies are initiated after seizure onset,[15–19] here, we tested whether expressing 4E-$BP1^{CA}$ in juvenile mice can reverse developmental phenotypes induced by embryonic $Rheb^{CA}$ expression.

The 4E-$BP1^{CA}$ construct used in these studies harbours a point mutation (F113A) that renders it resistant to phosphorylation and inactivation by mTORC1.[22,23] Expression of 4E-$BP1^{CA}$ in $Rheb^{CA}$-expressing HEK293T cells led to a decrease in cap-dependent translation as measured by a dual luciferase reporter assay, and the decrease was comparable to levels reduced by treatment with 250 nM Torin 1, a selective mTOR inhibitor and blocker of translation (Supplementary Fig. 2A and B and Supplementary Table 2). 4E-$BP1^{CA}$ expression did not alter the phosphorylation levels of S6 at S240/244 or AKT at S473, sites phosphorylated by mTORC1 and mTORC2, respectively (Supplementary Fig. 2C–E and Supplementary Table 2), confirming the specificity of 4E-$BP1^{CA}$ on downstream mTORC1/4E-BP-mediated functions.

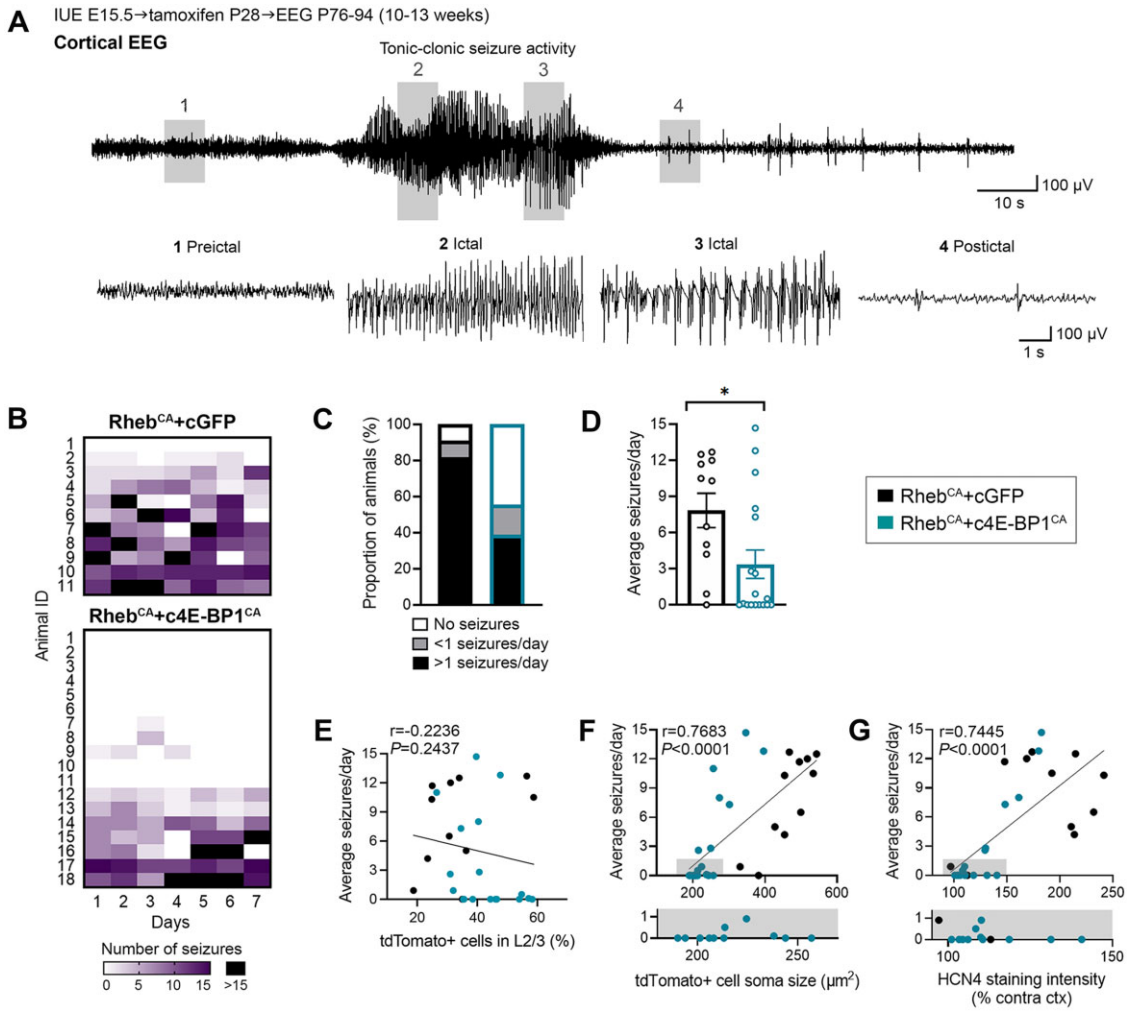

Figure 5 c4E-BP1^{CA} expression after epilepsy onset in juvenile Rheb^{CA} mice alleviates seizures. (**A**) Sample cortical EEG trace showing a typical seizure in Rheb^{CA} mice. Expanded EEG traces from representative preictal, ictal and postictal periods are shown at the *bottom*. (**B**) Heat map showing the daily number of seizures of individual animals over seven consecutive days of vEEG recording. (**C**) Bar graph showing the proportion of animals in each group with no seizures, <1 seizure/day and >1 seizure/day. $n = 11$ Rheb^{CA} + cGFP, $n = 18$ Rheb^{CA} + c4E-BP1^{CA} mice. (**D**) Quantification of seizure frequency. $n = 11$ Rheb^{CA} + cGFP, $n = 18$ Rheb^{CA} + c4E-BP1^{CA} mice; each data-point represents mean seizures/day over a 7-day recording period per animal. Data were analysed using Mann–Whitney U-test; *$P = 0.0206$. (**E–G**) Scatterplots of (**E**) seizure frequency versus cell placement in L2/3, (**F**) seizure frequency versus cell size and (**G**) seizure frequency versus HCN4 staining intensity. For plots (**F** and **G**), the areas denoted with the grey boxes are enlarged below to reveal overlapping values. $n = 29$ (**E** and **F**), $n = 28$ (**G**) XY pairs. Data were analysed with Spearman's rank-order correlation. Error bars are ± SEM.

To conditionally express 4E-BP1^{CA} in juvenile Rheb^{CA} mice, we co-electroporated Rheb^{CA} with a conditional 4E-BP1^{CA} (c4E-BP1^{CA}) plasmid, along with a tamoxifen-inducible Cre recombinase plasmid, by IUE. In the conditional cassette, 4E-BP1^{CA} is preceded by a loxP-flanked stop cassette that suppresses its expression. Upon tamoxifen administration, Cre recombinase mediates the excision of the stop cassette, allowing for 4E-BP1^{CA} to be expressed. To control for 4E-BP1^{CA} expression, a subset of mice was electroporated with the same plasmids as above but with a conditional GFP (cGFP) instead of c4E-BP1^{CA}. To control for Rheb^{CA} expression, a negative control group expressing BFP, cGFP and Cre recombinase was included. A tdTomato reporter plasmid was co-electroporated with all conditions to label targeted cells. Tamoxifen was administered from P12 to P16 in all mice to induce 4E-BP1^{CA} (or GFP) expression. By this age, multiple cellular phenotypes, including electrophysiological alterations, are present.[14] Whole-cell patch clamp recordings were obtained from L2/3 pyramidal neurons expressing Rheb^{CA} + c4E-BP1^{CA}, Rheb^{CA} + cGFP, or BFP + cGFP (hereafter referred to as control) in acute brain slices from P23–32 mice (Fig. 2A and B).

Consistent with the visible changes in neuron size, Rheb^{CA} + cGFP neurons displayed increased membrane capacitance which was partially rescued in Rheb^{CA} + c4E-BP1^{CA} neurons (Fig. 2B and C and Supplementary Table 1). Rheb^{CA} + cGFP neurons also had increased resting membrane conductance (Fig. 2D) and more depolarized RMP (Fig. 2E). c4E-BP1^{CA} expression normalized the RMP but not conductance (Fig. 2D and E and Supplementary Table 1).

We recently reported that Rheb^{CA} neurons have an abnormal expression of HCN4 channels, which give rise to a hyperpolarization-activated cation current (I_h) that is normally absent in L2/3 pyramidal neurons.[14] The presence of aberrant I_h, which has implications for neuronal excitability, preceded seizure onset and was detected by P8–12 in mice. Rapamycin treatment starting at P1 prevented the aberrant HCN4 channel expression, suggesting this is an mTORC1-dependent process. However, it is unknown whether HCN4 channel expression is regulated downstream through 4E-BPs and whether this electrophysiological alteration can be reversed. Thus, we examined the effects of c4E-BP1^{CA} expression on I_h. To evoke I_h, we applied a series of 3-s long hyperpolarizing voltage steps from –130 mV to –40 mV. Consistent with

previous findings,[14] hyperpolarizing voltage pulses elicited significantly larger inward currents in Rheb^{CA} + cGFP neurons compared to control neurons (Fig. 2F and G and Supplementary Table 1). The inward currents in Rheb^{CA} neurons result from the activation of both inward-rectifier K+ channels (K_{ir}) and HCN4 channels.[14] Because K_{ir}-mediated currents activate quickly whereas I_h activates slowly during hyperpolarizing steps, to assess I_h amplitudes, we measured the difference between the instantaneous and steady-state currents at the beginning and end of the voltage pulses, respectively (i.e. ΔI).[27,28] The resulting IV curve revealed significantly larger I_h amplitudes in Rheb^{CA} + cGFP neurons compared to control neurons, in which I_h was absent (Fig. 2H and Supplementary Table 1). These findings are best demonstrated at –90 mV, close to the reversal potential for K_{ir} channels, when no K_{ir} current is expected and the observed current is predominantly due to I_h (Fig. 2I, Supplementary Table 1). c4E-BP1^{CA} expression did not affect the overall inward current amplitudes (Fig. 2F and G and Supplementary Table 1) but significantly decreased I_h amplitudes (Fig. 2H, Supplementary Table 1) in Rheb^{CA} neurons. We did not detect changes in the overall inward current despite decreased I_h likely due to the small contribution of I_h to the overall inward current. At –90 mV, there were no differences in the mean I_h amplitudes between Rheb^{CA} + c4E-BP1^{CA} neurons and control neurons, indicating that c4E-BP1^{CA} expression restored the aberrant I_h expression (Fig. 2I and Supplementary Table 1). Consistent with the function of I_h in maintaining RMP at depolarized levels,[36–40] larger I_h amplitudes significantly correlated with more depolarized RMPs in the recorded neurons (Fig. 2J and Supplementary Table 1). In agreement with the data for I_h amplitudes, hyperpolarizing current injections in current clamp mode evoked a prominent I_h-mediated voltage sag in Rheb^{CA} + cGFP neurons, which was absent or minimal in control and Rheb^{CA} + c4E-BP1^{CA} neurons (Fig. 2K–M and Supplementary Table 1). Collectively, these findings demonstrate that c4E-BP1^{CA} expression rescues the aberrant I_h expression in Rheb^{CA} neurons.

To assess the effects of c4E-BP1^{CA} expression on intrinsic excitability, we examined the AP firing response to depolarizing current injections. We found no differences in AP threshold, peak amplitude, and half-width between the groups (Supplementary Fig. 3A–C and Supplementary Table 2). Rheb^{CA} + cGFP neurons fired fewer APs for current injections above 100 pA compared to control neurons. No differences in the AP input–output curve were found between Rheb^{CA} + cGFP and Rheb^{CA} + c4E-BP1^{CA} neurons, indicating that c4E-BP1^{CA} expression did not rescue the depolarization-induced firing frequency (Fig. 2N and O and Supplementary Table 1). In terms of firing pattern, neurons in all groups displayed a regular-spiking pattern with spike-frequency adaptation. However, while an initial doublet was observed in control neurons, consistent with the expected firing pattern for L2/3 mPFC pyramidal neurons,[41] this was absent in Rheb^{CA} + cGFP neurons and reflected by a notably longer first interspike interval (Fig. 2N). Quantification of interspike intervals in an adaptive train of ⩾10 spikes showed a significant increase in the first interspike interval in Rheb^{CA} + cGFP neurons that was normalized in Rheb^{CA} + c4E-BP1^{CA} neurons. In comparison, no changes in the ninth interspike interval were observed between the groups (Supplementary Fig. 3D and E and Supplementary Table 2). Overall, c4E-BP1^{CA} expression rescues the irregular firing pattern but not depolarization-induced firing frequency in Rheb^{CA} neurons.

c4E-BP1^{CA} expression in juvenile Rheb^{CA} mice reduces neuronal cytomegaly and aberrant HCN4 channel expression

Having established that c4E-BP1^{CA} expression corrects multiple electrophysiological deficits in Rheb^{CA} neurons, we next examined whether c4E-BP1^{CA} expression would also reverse mTORC1-induced histopathological abnormalities and whether this would be sufficient to rescue spontaneous seizure activity in Rheb^{CA} mice. In these experiments, we performed IUE with the same conditions as described above and administered tamoxifen from P28 to P32 to induce c4E-BP1^{CA} or cGFP expression (Fig. 3A). By this age, FMCD pathology, including neuron misplacement and cytomegaly, is fully established.[13,30,34,35] Rheb^{CA} mice begin to exhibit seizures by P21–P28, and the timeline for tamoxifen administration was chosen to allow the animals to become symptomatic prior to inducing 4E-BP1^{CA} expression. Mice were recorded with vEEG starting at P76–94 (10–13 weeks of age) and brain tissues were afterward collected for histological examination at P84–106 (12–15 weeks of age).

We first examined the effects of c4E-BP1^{CA} expression on core FMCD cytoarchitectural abnormalities. We found no changes in Rheb^{CA} neuron placement following c4E-BP1^{CA} expression. In both groups, the electroporated neurons were found misplaced across the cortex and only ∼40% were correctly located in L2/3 (Fig. 3B and C and Supplementary Table 1). Some cells were ectopically found in the white matter near the corpus callosum; this type of heterotopia was found in both groups and the degree of heterotopia was variable between animals in both conditions (Fig. 3B). In contrast, c4E-BP1^{CA} expression significantly decreased the soma size of Rheb^{CA} neurons (Fig. 3B and D and Supplementary Table 1). The mean soma size in a group of Rheb^{CA} + c4E-BP1^{CA} mice that received vehicle instead of tamoxifen treatment was not different from that in Rheb^{CA} + cGFP mice, validating that the c4E-BP1^{CA} plasmid did not have leaky expression and the effects on neuron size require Cre-mediated c4E-BP1^{CA} expression (Supplementary Fig. 4A and B and Supplementary Table 2). Taken together, these findings show that c4E-BP1^{CA} expression in juvenile Rheb^{CA} mice reduces neuronal cytomegaly but not misplacement.

Given that c4E-BP1^{CA} expression normalized the aberrant I_h in Rheb^{CA} neurons, we sought to further evaluate the expression of HCN channels by immunostaining. There are four HCN isoforms in the brain; HCN1 and HCN2 are highly expressed in the cortex and hippocampus, whereas HCN3 and HCN4 are predominantly found in the subcortical regions.[42,43] Within the cortex, HCN1 and 2 are expressed in the deeper layer pyramidal neurons, while no functional HCN channels are found in L2/3 pyramidal neurons.[41] We found no differences in HCN1–3 staining between the hemispheres or animal groups (Supplementary Fig. 5A–F and Supplementary Table 2). In contrast, we observed a significant increase in HCN4 staining intensity on the ipsilateral (electroporated) side compared to the contralateral side of the cortex in Rheb^{CA} + cGFP mice (Fig. 3E and F and Supplementary Table 1). The overall staining pattern was diffuse with some neurons exhibiting bright somatic staining (Fig. 3E). The increase in HCN4 staining intensity was significantly reduced by c4E-BP1^{CA} expression (Fig. 3E and F and Supplementary Table 1), suggesting that the c4E-BP1^{CA}-mediated rescue of I_h results from decreased HCN4 channel expression. In both groups, strong HCN4 staining was present in the medial septum where these channels are normally expressed,[42] serving as an internal staining control (Fig. 3E). The reduction in cortical HCN4 staining intensity was not detected in vehicle-treated Rheb^{CA} + c4E-BP1^{CA} mice, supporting that the effects on HCN4 channel expression result from c4E-BP1^{CA} expression (Supplementary Fig. 5G and H and Supplementary Table 2). Collectively, these findings demonstrate that c4E-BP1^{CA} expression in juvenile Rheb^{CA} mice decreases aberrant HCN4 channel expression, consistent with the functional reduction in I_h.

c4E-BP1^{CA} expression after epilepsy onset in juvenile Rheb^{CA} mice normalizes cortical spectral activity and alleviates seizures

Considering the electrophysiological and morphological rescue following c4E-BP1^{CA} expression, we examined whether c4E-BP1^{CA}

expression in juvenile Rheb^{CA} mice would improve cortical EEG activity and reduce spontaneous seizures in adults. For these studies, the same animals from Fig. 3 were used. The majority of these mice (6/11 Rheb^{CA} + cGFP, 14/18 Rheb^{CA} + c4E-BP1^{CA} mice) exhibited visible tonic–clonic seizures prior to or during tamoxifen administration from P28 to P35; thus, epilepsy was already manifested by the time c4E-BP1^{CA} expression was induced. Continuous vEEG recording was performed 6–8 weeks post-tamoxifen administration, starting at P76–94, for 7 days to monitor cortical activity and seizure behaviours.

To examine cortical activity, we characterized the background EEG activity using spectral power analysis. This quantitative EEG method uses non-biased signal processing to decompose raw EEG waves into discrete frequency bands and provides a neurophysiological measure of brain state and network function.[44–46] Data were analysed during the light and dark cycles to account for any circadian variables and were compared to a control group expressing GFP only. Rheb^{CA} + cGFP mice displayed a significant upward shift in the relative power spectrum compared to control mice during light cycle activity. The shift was primarily observed in the higher frequency range of beta and gamma activity. No differences were observed between Rheb^{CA} + c4E-BP1^{CA} and control mice, suggesting that c4E-BP1^{CA} expression normalized relative spectral power (Fig. 4A and B and Supplementary Table 1). Consistent with these findings, relative bandpower analysis revealed increased beta activity in Rheb^{CA} + cGFP mice, which was restored to control levels in Rheb^{CA} + c4E-BP1^{CA} mice. Gamma activity was also higher in Rheb^{CA} + cGFP mice than Rheb^{CA} + c4E-BP1^{CA} mice, although neither group was statistically different from control mice (Fig. 4D and E and Supplementary Table 1). No differences in the dark cycle relative power spectrum or bandpower were observed between the groups (Fig. 4A, C and F and Supplementary Table 1). Overall, these data demonstrate the presence of altered cortical spectral activity in Rheb^{CA} mice, which is restored by juvenile c4E-BP1^{CA} expression.

We next quantified the incidence and frequency of spontaneous seizures (Fig. 5A). We found a marked reduction in the percentage of mice with seizure activity in the Rheb^{CA} + c4E-BP1^{CA} group. Comparing the portion of Rheb^{CA} + c4E-BP1^{CA} mice to that of Rheb^{CA} + cGFP mice, 44% versus 9% displayed no seizures, 17% versus 9% had <1 seizures/day and 39% versus 82% had >1 seizures/day (Fig. 5B and C). The frequency of daily seizures was significantly decreased by $>50\%$ in Rheb^{CA} + c4E-BP1^{CA} mice compared to Rheb^{CA} + cGFP mice (Fig. 5D and Supplementary Table 1). These Rheb^{CA} + c4E-BP1^{CA} mice (i.e. tamoxifen-treated) also had fewer seizures compared to littermate Rheb^{CA} + c4E-BP1^{CA} mice that received vehicle treatment (Supplementary Fig. 6 and Supplementary Table 2). Together, these findings support that c4E-BP1^{CA} expression after epilepsy onset in juvenile Rheb^{CA} mice attenuates seizures.

Within both animal groups, we observed a broad range of seizure frequencies. To determine whether there was a relationship between individual animal seizure frequency and mTORC1-induced histopathological abnormalities, we correlated seizure frequency with the corresponding data for neuron placement, soma size and HCN4 staining intensity as reported in Fig. 3 for each animal. We found no correlation between seizure frequency and neuron placement (Fig. 5E and Supplementary Table 1). In contrast, seizure frequency positively correlated with soma size and HCN4 staining intensity (Fig. 5F and G and Supplementary Table 1). Based on these findings, we separated the HCN4 data from Fig. 3 by seizure activity and found that Rheb^{CA} + c4E-BP1^{CA} mice with <1 seizure/day had a complete rescue of HCN4 levels while those with >1 seizure/day had significantly elevated HCN4 levels (Supplementary Fig. 7 and Supplementary Table 2). Taken together, these findings show that c4E-BP1^{CA}-mediated reduction of seizure activity is associated with an improvement in neuron cytomegaly and aberrant HCN4 channel expression. Further, they show that c4E-BP1^{CA} expression attenuates seizures independently of neuron placement.

Discussion

Growing evidence supports mTORC1 pathway-activating mutations as a major genetic cause for FMCD and intractable epilepsy, and understanding the mTORC1 downstream mechanisms that contribute to the pathology is crucial for developing new therapeutics. Here, we have identified the mTORC1-regulated translational repressor 4E-BP1 as a critical contributor to neuronal dysfunction and epilepsy. Our study is the first to demonstrate the reversibility of specific mTORC1-induced developmental alterations in neuron electrophysiological function and morphology by juvenile genetic manipulation of 4E-BP1 in mice. These findings have clinical relevance and support targeting 4E-BP1 as a potential treatment strategy for epilepsy in mTORC1-related FMCDs.

Dysmorphic FMCD neurons from TSC and FCDII patients and Rheb^{CA} mice display increased levels of phosphorylated 4E-BP1, consistent with previous reports in human TSC, FCDII and HME brain specimens[11,47–49] and other FMCD mouse models with mTORC1 hyperactivation.[11,50,51] The presence of hyperphosphorylated 4E-BP1 implicates inhibited repressor activity, and thus, overactive translation. Recent work by Kim *et al.*[11] reported increased translation of >200 mTOR-dependent genes with functions in epileptic seizures, dysmorphogenesis and mislamination in cortical neurons from FMCD mice carrying brain somatic *mTOR* mutations. Reducing translation by eIF4E inhibition during foetal neurodevelopment rescued FMCD pathology and seizures, supporting dysregulated translation as a mechanism underlying FMCD and epilepsy.[11] Our study is in agreement with these findings and further supports the role of translational dysregulation in epilepsy.

With regards to therapies for epilepsy, adult treatment with metformin, a widely used antidiabetic drug also known to inhibit mTORC1-mediated translation via AMP-activated protein kinase activation,[52] has been shown to decrease seizures in a mouse model of FMCD mice.[11] However, metformin activates multiple targets[53] and has various effects in the brain, including inhibiting ERK signalling,[54] enhancing cerebral angiogenesis and neurogenesis,[55,56] decreasing glial activation and suppressing inflammatory pathways[57,58] and altering the gut microbiome,[59] and it is unclear whether the mechanism of action was through inhibiting translation. In this study, we provide direct genetic support for reducing overactive translation via 4E-BP1 to alleviate established epilepsy. Given the recent advances in gene therapy for neurodevelopmental disorders,[60–62] correcting translational dysregulation by 4E-BP1^{CA}-targeted gene therapy may be a feasible treatment strategy for genetically defined FMCDs.

Hyperactivation of mTORC1 signalling during neurodevelopment impairs cortical neuron migration and morphogenesis, resulting in neuronal misplacement across the cortical layer and cytomegaly. These FMCD hallmarks are consistently recapitulated in all current FMCD mouse models with mTORC1 hyperactivity.[7] Induction of c4E-BP1^{CA} expression at P28 in Rheb^{CA} mice was sufficient to reduce neuronal cytomegaly, but not misplacement. This latter finding is expected because pyramidal neurons reach their final position in the cortex by P7–10.[63,64] At the behavioural level, c4E-BP1^{CA} expression improved cortical spectral activity and decreased seizures. Thus, our findings suggest that correcting or attenuating specific morphological and functional alterations can alleviate FMCD-related epilepsy, even if the associated neuroanatomical defects are not reversed.

Few studies have examined the changes in intrinsic electrophysiological properties in cortical pyramidal neurons following mTORC1 hyperactivation, and even fewer studies have done this in the mPFC. We recently reported a set of electrophysiological alterations in mPFC Rheb^{CA} neurons that includes depolarized RMP, increased resting membrane conductance resulting from increased K_{ir} current and I_h due to abnormal HCN4 channel expression and reduced firing frequency upon depolarizing current injections.[14] Here, we recapitulated these results and additionally report changes in Rheb^{CA} neuron firing pattern characterized by loss of an initial doublet firing. c4E-BP1^{CA} expression restored RMP and the firing pattern and removed aberrant I_h in Rheb^{CA} neurons, suggesting that these alterations are 4E-BP1-dependent. In contrast, c4E-BP1^{CA} expression did not rescue the K_{ir} current or depolarization-induced firing frequency, suggesting that other processes contribute to these changes. The aberrant expression of HCN4 channels has notable implications for Rheb^{CA} neuron excitability and firing. Despite these neurons having decreased depolarization-induced excitability, the aberrant presence of HCN4 channels drives firing through a cAMP-dependent process and silencing HCN4 channels was sufficient to reduce seizure activity in mice.[14] Thus, 4E-BP1^{CA}-mediated removal of aberrant HCN4 channels potentially contributes to seizure reduction. Similar to Rheb^{CA} neurons, FMCD pyramidal neurons expressing other mTORC1-activating variants, including another Rheb variant, *Rheb Y35L*, *mTOR L2427P*, *Tsc1* and *Depdc5* knockouts, also display decreased depolarization-induced firing responses.[65–68] How these neurons lead to hyperexcitability and seizures is unknown. Our data suggest that aberrant acquisition of HCN4 channels may be a shared mode of abnormal excitability in these neurons. Nevertheless, whether aberrant HCN4 channel expression occurs in these other gene variants remains to be examined.

To our knowledge, no other studies have characterized the background EEG activity of FMCD mouse models by spectral analysis. EEG waves, reflecting rhythmic neuronal network activity in the brain, oscillate in various frequency bands that correlate with specific physiological functions and behavioural states.[69] Quantification of EEG activity by spectral power analysis has been used clinically to aid in the diagnosis and evaluation of cortical activity and disease severity, as well as assessing therapeutics, in neurocognitive and psychiatric disorders.[70–76] Remarkably, despite Rheb^{CA} being expressed in a relatively small fraction of neurons and a limited area of the cortex, this was sufficient to induce detectable changes in cortical spectral activity. In particular, we found increased beta activity in Rheb^{CA} mice that was restored by c4E-BP1^{CA} expression. Interestingly, altered resting-state functional connectivity with increased beta and gamma bands has been reported in human FCD.[77,78] Beta waves are associated with cortical activation and high arousal states, and excessive beta activity has been implicated in stress, anxiety, insomnia and attention deficit hyperactivity disorder.[79–82] Therefore, increased beta activity in Rheb^{CA} mice could reflect the presence of these behaviours. Neuropsychiatric comorbidities such as sleep disruption are common in human TSC and childhood epilepsy[83–86] and have been described in a TSC mouse model.[87] Notably, alterations in Rheb^{CA} mice beta activity were only observed during the light cycle, when mice generally spend more time in rest and sleep, but not during the dark cycle, when mice are awake. This could hint at a disturbance in normal sleep activity in Rheb^{CA} mice; however, additional in-depth sleep analysis using EMG recording will be required to examine this.

Overall, our study demonstrates that although mTORC1 activates multiple molecular pathways, remarkably, restoring 4E-BP1 function is sufficient to improve many aspects of the disorder, including neuron cytomegaly, electrophysiological impairments, cortical spectral dysfunction and epilepsy. Here, we did not examine the effects of c4E-BP1^{CA} expression on dendritic and synaptic function or axonal activity. Alterations in these parameters, which contribute to local or long-range alterations in connectivity and excitability, have been reported in FMCD neurons with mTORC1 hyperactivation.[12,13,65,66,68,88,89] Thus, it is possible that c4E-BP1^{CA} expression also impacts dendritic and axonal function, leading to attenuated epilepsy. Furthermore, while our data underscore that many alterations can be rescued by c4E-BP1^{CA} expression, it should not be inferred that dysregulated 4E-BP1 activity alone causes epilepsy. A recent study showed that ablation of 4E-BP2, but not 4E-BP1, reduces the threshold to chemoconvulsant-induced seizures in mice, although neither resulted in spontaneous seizure activity.[90] Interestingly, the effects on seizure threshold were specific to 4E-BP2 deletion in parvalbumin inhibitory neurons and not in other inhibitory or excitatory neurons in the hippocampus. Data from that study suggest that inhibiting 4E-BP1 or 4E-BP2 function in pyramidal neurons may not be sufficient to trigger seizures. This further supports the notion that a combination of molecular alterations downstream of mTORC1 is necessary to induce seizures; however, rescuing one molecular alteration is sufficient to alleviate the seizure burden.

In conclusion, we show that targeting 4E-BP1 after the underlying circuit abnormalities are established corrects multiple mTORC1-induced neuronal phenotypes and alleviates epilepsy. Our findings support the emerging notion that dysregulated translation is a major contributor to FMCD and epilepsy. Finally, targeting 4E-BP1 *via* gene therapy may represent a treatment strategy for epilepsy in mTORC1-related FMCD.

Acknowledgements

We thank the Tuberous Sclerosis Complex Alliance for providing one of the human TSC specimens.

Funding

This work was supported by the National Institute of Neurological Disorders and Stroke R01 NS086329, NS111980 (A.B.), Eunice Kennedy Shriver National Institute of Child Health and Human Development F32 HD095567 (L.H.N.), American Epilepsy Society Postdoctoral Fellowship (L.H.N.), Yale Brown Coxe Postdoctoral Fellowship (L.H.N.) and Swebilius Foundation Grant (L.H.N.).

Competing interests

LHN and AB are co-inventors on a patent application, PCT/US2020/054007 entitled “Targeting Cap-Dependent Translation to Reduce Seizures in mTOR disorders”. AB is an inventor on two patent applications, PCT/US2020/020994 entitled “Methods of Treating and Diagnosing Epilepsy” and PCT/US2020/018136 entitled “Methods of Treating Epilepsy”.

Supplementary material

Supplementary material is available at *Brain* online.

References

1. Crino PB. mTOR signaling in epilepsy: Insights from malformations of cortical development. *Cold Spring Harb Perspect Med*. 2015;5(4):a022442-1.

2. Kwiatkowski DJ. Tuberous sclerosis: From tubers to mTOR. *Ann Hum Genet*. 2003;67(Pt 1):87–96.
3. Marsan E, Baulac S. Review: Mechanistic target of rapamycin (mTOR) pathway, focal cortical dysplasia and epilepsy. *Neuropathol Appl Neurobiol*. 2018;44(1):6–17.
4. Muhlebner A, Bongaarts A, Sarnat HB, Scholl T, Aronica E. New insights into a spectrum of developmental malformations related to mTOR dysregulations: Challenges and perspectives. *J Anat*. 2019;235(3):521–542.
5. Lim KC, Crino PB. Focal malformations of cortical development: New vistas for molecular pathogenesis. *Neuroscience*. 2013;252: 262–276.
6. Ostendorf AP, Wong M. mTOR inhibition in epilepsy: Rationale and clinical perspectives. *CNS Drugs*. 2015;29(2):91–9.
7. Nguyen LH, Bordey A. Convergent and divergent mechanisms of epileptogenesis in mTORopathies. *Front Neuroanat*. 2021;15: 664695.
8. Lipton JO, Sahin M. The neurology of mTOR. *Neuron*. 2014;84(2): 275–291.
9. Saxton RA, Sabatini DM. mTOR signaling in growth, metabolism, and disease. *Cell*. 2017;169(2):361–371.
10. Lasarge CL, Danzer SC. Mechanisms regulating neuronal excitability and seizure development following mTOR pathway hyperactivation. *Front Mol Neurosci*. 2014;7:18.
11. Kim JK, Cho J, Kim SH, et al. Brain somatic mutations in MTOR reveal translational dysregulations underlying intractable focal epilepsy. *J Clin Invest*. 2019;129(10):4207–4223.
12. Gong X, Zhang L, Huang T, et al. Activating the translational repressor 4E-BP or reducing S6K-GSK3beta activity prevents accelerated axon growth induced by hyperactive mTOR *in vivo*. *Hum Mol Genet*. 2015;24(20):5746–5758.
13. Lin TV, Hsieh L, Kimura T, Malone TJ, Bordey A. Normalizing translation through 4E-BP prevents mTOR-driven cortical mislamination and ameliorates aberrant neuron integration. *Proc Natl Acad Sci*. 2016;113(40):11330–11335.
14. Hsieh LS, Wen JH, Nguyen LH, et al. Ectopic HCN4 expression drives mTOR-dependent epilepsy in mice. *Sci Transl Med*. 2020; 12(570):eabc1492.
15. Staley BA, Vail EA, Thiele EA. Tuberous sclerosis complex: Diagnostic challenges, presenting symptoms, and commonly missed signs. *Pediatrics*. 2011;127(1):e117–e125.
16. Kabat J, Krol P. Focal cortical dysplasia—Review. *Pol J Radiol*. 2012;77(2):35–43.
17. Ebrahimi-Fakhari D, Mann LL, Poryo M, et al. Incidence of tuberous sclerosis and age at first diagnosis: New data and emerging trends from a national, prospective surveillance study. *Orphanet J Rare Dis*. 2018;13(1):117.
18. Racz A, Muller AM, Schwerdt J, Becker A, Vatter H, Elger CE. Age at epilepsy onset in patients with focal cortical dysplasias, gangliogliomas and dysembryoplastic neuroepithelial tumours. *Seizure*. 2018;58:82–89.
19. Oegema R, Barakat TS, Wilke M, et al. International consensus recommendations on the diagnostic work-up for malformations of cortical development. *Nat Rev Neurol*. 2020;16(11):618–635.
20. Richter JD, Sonenberg N. Regulation of cap-dependent translation by eIF4E inhibitory proteins. *Nature*. 2005;433(7025):477–80.
21. Ma XM, Blenis J. Molecular mechanisms of mTOR-mediated translational control. *Nat Rev Mol Cell Biol*. 2009;10(5):307–318.
22. Choi KM, McMahon LP, Lawrence JC Jr. Two motifs in the translational repressor PHAS-I required for efficient phosphorylation by mammalian target of rapamycin and for recognition by raptor. *J Biol Chem*. 2003;278(22):19667–19673.
23. Schalm SS, Fingar DC, Sabatini DM, Blenis J. TOS motif-mediated raptor binding regulates 4E-BP1 multisite phosphorylation and function. *Curr Biol*. 2003;13(10):797–806.
24. Maehama T, Tanaka M, Nishina H, Murakami M, Kanaho Y, Hanada K. RalA functions as an indispensable signal mediator for the nutrient-sensing system. *J Biol Chem*. 2008;283(50): 35053–35059.
25. Breunig JJ, Gate D, Levy R, et al. Rapid genetic targeting of pial surface neural progenitors and immature neurons by neonatal electroporation. *Neural Dev*. 2012;7:26.
26. Pathania M, Torres-Reveron J, Yan L, et al. miR-132 enhances dendritic morphogenesis, spine density, synaptic integration, and survival of newborn olfactory bulb neurons. *PLoS One*. 2012; 7(5):e38174.
27. Fan J, Stemkowski PL, Gandini MA, et al. Reduced hyperpolarization-activated current contributes to enhanced intrinsic excitability in cultured hippocampal neurons from PrP(–/–) Mice. *Front Cell Neurosci*. 2016;10:74.
28. Thoby-Brisson M, Telgkamp P, Ramirez JM. The role of the hyperpolarization-activated current in modulating rhythmic activity in the isolated respiratory network of mice. *J Neurosci*. 2000;20(8):2994–3005.
29. George MS, Abbott LF, Siegelbaum SA. HCN hyperpolarization-activated cation channels inhibit EPSPs by interactions with M-type K(+) channels. *Nat Neurosci*. 2009;12(5):577–584.
30. Nguyen LH, Mahadeo T, Bordey A. mTOR hyperactivity levels influence the severity of epilepsy and associated neuropathology in an experimental model of tuberous sclerosis complex and focal cortical dysplasia. *J Neurosci*. 2019;39(14):2762–2773.
31. Sisodiya SM, Fauser S, Cross JH, Thom M. Focal cortical dysplasia type II: Biological features and clinical perspectives. *Lancet Neurol*. 2009;8(9):830–843.
32. Blumcke I, Thom M, Aronica E, et al. The clinicopathologic spectrum of focal cortical dysplasias: A consensus classification proposed by an *ad hoc* Task Force of the ILAE Diagnostic Methods Commission. *Epilepsia*. 2011;52(1):158–174.
33. Sousa GK, Capitelli CS, Dombroski TCD, et al. Identification and immunophenotype of abnormal cells present in focal cortical dysplasia type IIb. Report. *Surg Exp Pathol*. 2018/12/20///2018;1: NA.
34. Hsieh LS, Wen JH, Claycomb K, et al. Convulsive seizures from experimental focal cortical dysplasia occur independently of cell misplacement. *Nat Commun*. 2016;7:11753.
35. Zhang L, Huang T, Teaw S, et al. Filamin A inhibition reduces seizure activity in a mouse model of focal cortical malformations. *Sci Transl Med*. 2020;12(531):eaay0289.
36. Doan TN, Kunze DL. Contribution of the hyperpolarization-activated current to the resting membrane potential of rat nodose sensory neurons. *J Physiol*. 1999;514(Pt 1):125–138.
37. Funahashi M, Mitoh Y, Kohjitani A, Matsuo R. Role of the hyperpolarization-activated cation current (I_h) in pacemaker activity in area postrema neurons of rat brain slices. *J Physiol*. 2003; 552(Pt 1):135–148.
38. Kase D, Imoto K. The role of HCN channels on membrane excitability in the nervous system. *J Signal Transduct*. 2012;2012: 619747.
39. Lamas JA. A hyperpolarization-activated cation current (I_h) contributes to resting membrane potential in rat superior cervical sympathetic neurones. *Pflugers Arch*. 1998;436(3):429–435.
40. Lupica CR, Bell JA, Hoffman AF, Watson PL. Contribution of the hyperpolarization-activated current (I(h)) to membrane potential and GABA release in hippocampal interneurons. *J Neurophysiol*. 2001;86(1):261–268.
41. Kroon T, van Hugte E, van Linge L, Mansvelder HD, Meredith RM. Early postnatal development of pyramidal neurons across layers of the mouse medial prefrontal cortex. *Sci Rep*. 2019;9(1): 5037.

42. Notomi T, Shigemoto R. Immunohistochemical localization of I_h channel subunits, HCN1–4, in the rat brain. *J Comp Neurol*. 2004;471(3):241–276.
43. Oyrer J, Bleakley LE, Richards KL, et al. Using a multiplex nucleic acid in situ hybridization technique to determine HCN4 mRNA expression in the adult rodent brain. *Front Mol Neurosci*. 2019;12: 211.
44. Welch PD. The use of fast fourier transform for the estimation of power spectra: A method based on time averaging over short, modified periodograms. *IEEE Trans Audio Electroacoust*. 1967; 15(2):70–73.
45. Schnitzler A, Gross J. Normal and pathological oscillatory communication in the brain. *Nat Rev Neurosci*. 2005;6(4):285–296.
46. Kim D-W, Im C-H. EEG spectral analysis. In: Im C-H, ed. *Computational EEG analysis: Methods and applications*. Springer Singapore; 2018: 35–53.
47. Baybis M, Yu J, Lee A, et al. mTOR cascade activation distinguishes tubers from focal cortical dysplasia. *Ann Neurol*. 2004; 56(4):478–487.
48. Orlova KA, Crino PB. The tuberous sclerosis complex. *Ann N Y Acad Sci*. 2010;1184:87–105.
49. Hanai S, Sukigara S, Dai H, et al. Pathologic active mTOR mutation in brain malformation with intractable epilepsy leads to cell-autonomous migration delay. *Am J Pathol*. 2017;187(5): 1177–1185.
50. Kassai H, Sugaya Y, Noda S, et al. Selective activation of mTORC1 signaling recapitulates microcephaly, tuberous sclerosis, and neurodegenerative diseases. *Cell Rep*. 2014;7(5): 1626–1639.
51. Koene LMC, van Grondelle SE, Onori MP, et al. Effects of antiepileptic drugs in a new TSC/mTOR-dependent epilepsy mouse model. *Ann Clin Transl Neur*. 2019;6(7):1273–1291.
52. Dowling RJ, Zakikhani M, Fantus IG, Pollak M, Sonenberg N. Metformin inhibits mammalian target of rapamycin-dependent translation initiation in breast cancer cells. *Cancer Res*. 2007; 67(22):10804–10812.
53. Viollet B, Guigas B, Sanz Garcia N, Leclerc J, Foretz M, Andreelli F. Cellular and molecular mechanisms of metformin: An overview. *Clin Sci (Lond)*. 2012;122(6):253–70.
54. Gantois I, Khoutorsky A, Popic J, et al. Metformin ameliorates core deficits in a mouse model of fragile X syndrome. *Nat Med*. 2017;23(6):674–677.
55. Wang J, Gallagher D, DeVito LM, et al. Metformin activates an atypical PKC-CBP pathway to promote neurogenesis and enhance spatial memory formation. *Cell Stem Cell*. 2012;11(1): 23–35.
56. Zhu X, Shen J, Feng S, et al. Metformin improves cognition of aged mice by promoting cerebral angiogenesis and neurogenesis. *Aging (Albany NY)*. 2020;12(18):17845–17862.
57. Ismaiel AA, Espinosa-Oliva AM, Santiago M, et al. Metformin, besides exhibiting strong *in vivo* anti-inflammatory properties, increases mptp-induced damage to the nigrostriatal dopaminergic system. *Toxicol Appl Pharmacol*. 2016;298:19–30.
58. Zhu XC, Jiang T, Zhang QQ, et al. Chronic metformin preconditioning provides neuroprotection via suppression of NF-kappaB-mediated inflammatory pathway in rats with permanent cerebral ischemia. *Mol Neurobiol*. 2015;52(1):375–385.
59. Wu H, Esteve E, Tremaroli V, et al. Metformin alters the gut microbiome of individuals with treatment-naive type 2 diabetes, contributing to the therapeutic effects of the drug. *Nat Med*. 2017;23(7):850–858.
60. Cheah PS, Prabhakar S, Yellen D, et al. Gene therapy for tuberous sclerosis complex type 2 in a mouse model by delivery of AAV9 encoding a condensed form of tuberin. *Sci Adv*. 2021;7(2): eabb1703.
61. Deverman BE, Ravina BM, Bankiewicz KS, Paul SM, Sah DWY. Gene therapy for neurological disorders: Progress and prospects. *Nat Rev Drug Discov*. 2018;17(10):767.
62. Turner TJ, Zourray C, Schorge S, Lignani G. Recent advances in gene therapy for neurodevelopmental disorders with epilepsy. *J Neurochem*. 2021;157(2):229–262.
63. Greig LC, Woodworth MB, Galazo MJ, Padmanabhan H, Macklis JD. Molecular logic of neocortical projection neuron specification, development and diversity. *Nat Rev Neurosci*. 2013;14(11):755–769.
64. Kast RJ, Levitt P. Precision in the development of neocortical architecture: From progenitors to cortical networks. *Prog Neurobiol*. 2019;175:77–95.
65. Ribierre T, Deleuze C, Bacq A, et al. Second-hit mosaic mutation in mTORC1 repressor DEPDC5 causes focal cortical dysplasia-associated epilepsy. *J Clin Invest*. 2018;128(6):2452–2458.
66. Onori MP, Koene LMC, Schafer CB, et al. RHEB/mTOR-hyperactivity causing cortical malformations drives seizures through increased axonal connectivity. *bioRxiv*. [Preprint] doi:10.1101/2020.07.08.189399
67. Goz RU, Akgul G, LoTurco JJ. BRAFV600E expression in neural progenitors results in a hyperexcitable phenotype in neocortical pyramidal neurons. *J Neurophysiol*. 2020;123(6):2449–2464.
68. Koh HY, Jang J, Ju SH, et al. Non-cell autonomous epileptogenesis in focal cortical dysplasia. *Ann Neurol*. 2021;90(2):285–299.
69. Buzsaki G, Watson BO. Brain rhythms and neural syntax: Implications for efficient coding of cognitive content and neuropsychiatric disease. *Dialogues Clin Neurosci*. 2012;14(4):345–367. Dec
70. Fonseca LC, Tedrus GM, Chiodi MG, Cerqueira JN, Tonelotto JM. Quantitative EEG in children with learning disabilities: Analysis of band power. *Arq Neuropsiquiatr*. 2006;64(2B):376–381.
71. Kanda PAM, Anghinah R, Smidth MT, Silva JM. The clinical use of quantitative EEG in cognitive disorders. *Dement Neuropsychol*. 2009;3(3):195–203.
72. Chiarenza GA, Chabot R, Isenhart R, et al. The quantified EEG characteristics of responders and non-responders to long-term treatment with atomoxetine in children with attention deficit hyperactivity disorders. *Int J Psychophysiol*. 2016;104:44–52.
73. Franko E, Wehner T, Joly O, et al. Quantitative EEG parameters correlate with the progression of human prion diseases. *J Neurol Neurosurg Psychiatry*. 2016;87(10):1061–1067.
74. Sidorov MS, Deck GM, Dolatshahi M, et al. Delta rhythmicity is a reliable EEG biomarker in Angelman syndrome: A parallel mouse and human analysis. *J Neurodev Disord*. 2017;9:17.
75. Roche KJ, LeBlanc JJ, Levin AR, O'Leary HM, Baczewski LM, Nelson CA. Electroencephalographic spectral power as a marker of cortical function and disease severity in girls with Rett syndrome. *J Neurodev Disord*. 2019;11(1):15.
76. Martinez LA, Born HA, Harris S, et al. Quantitative EEG Analysis in Angelman Syndrome: Candidate method for assessing therapeutics. *Clin EEG Neurosci*. Published online 18 November 2020. doi:10.1177/1550059420973095
77. Jeong W, Jin SH, Kim M, Kim JS, Chung CK. Abnormal functional brain network in epilepsy patients with focal cortical dysplasia. *Epilepsy Res*. 2014;108(9):1618–1626.
78. Jin SH, Jeong W, Chung CK. Focal cortical dysplasia alters electrophysiological cortical hubs in the resting-state. *Clin Neurophysiol*. 2015;126(8):1482–1492.
79. Clarke AR, Barry RJ, Heaven PC, McCarthy R, Selikowitz M, Byrne MK. EEG in adults with attention-deficit/hyperactivity disorder. *Int J Psychophysiol*. 2008;70(3):176–183.
80. Clarke AR, Barry RJ, McCarthy R, Selikowitz M. Excess beta activity in children with attention-deficit/hyperactivity disorder: An atypical electrophysiological group. *Psychiatry Res*. 2001; 103(2-3):205–218.

81. Perlis ML, Merica H, Smith MT, Giles DE. Beta EEG activity and insomnia. *Sleep Med Rev*. 2001;5(5):363–374.
82. Engel AK, Fries P. Beta-band oscillations–Signalling the *status quo*? *Curr Opin Neurobiol*. 2010;20(2):156–165.
83. Hunt A. Development, behaviour and seizures in 300 cases of tuberous sclerosis. *J Intellect Disabil Res*. 2008;37(1):41–51.
84. Tsai SY, Lee WT, Jeng SF, Lee CC, Weng WC. Sleep and behavior problems in children with epilepsy. *J Pediatr Health Care*. 2019; 33(2):138–145.
85. Hunt A, Stores G. Sleep disorder and epilepsy in children with tuberous sclerosis: A questionnaire-based study. *Dev Med Child Neurol. Feb*. 1994;36(2):108–115.
86. Bruni O, Cortesi F, Giannotti F, Curatolo P. Sleep disorders in tuberous sclerosis: A polysomnographic study. *Brain Dev*. 1995; 17(1):52–56.
87. Zhang B, Guo D, Han L, Rensing N, Satoh A, Wong M. Hypothalamic orexin and mechanistic target of rapamycin activation mediate sleep dysfunction in a mouse model of tuberous sclerosis complex. *Neurobiol Dis*. 2020;134:104615.
88. Zhong S, Zhao Z, Xie W, et al. GABAergic interneuron and neurotransmission are mTOR-dependently disturbed in experimental focal cortical dysplasia. *Mol Neurobiol*. 2021;58(1): 156–169.
89. Chen F, Rosiene J, Che A, Becker A, LoTurco J. Tracking and transforming neocortical progenitors by CRISPR/Cas9 gene targeting and piggyBac transposase lineage labeling. *Development*. 2015;142(20):3601–3611.
90. Sharma V, Sood R, Lou D, et al. 4E-BP2-dependent translation in parvalbumin neurons controls epileptic seizure threshold. *Proc Natl Acad Sci USA*. 2021;118(15):e2025522118.